# Numerical investigation of the flow inside a precession driven cylindrical cavity with additional baffles using an Immersed Boundary Method

Wilbert, M.; Giesecke, A.; Grauer, R.;

Originally published:

September 2022

**Physics of Fluids 34(2022), 096607**

DOI: https://doi.org/10.1063/5.0110153

Accepted to Phys. Fluids 10.1063/5.0110153

# Numerical investigation of the flow inside a precession driven cylindrical cavity with additional baffles using an Immersed Boundary Method

Mike Wilbert,[1, a)] André Giesecke,[2] and Rainer Grauer[1]
[1)] *Institut für Theoretische Physik I, Ruhr-Universität Bochum, D-44780 Bochum, Germany*
[2)] *Helmholtz-Zentrum Dresden–Rossendorf, Institute of Fluid Dynamics, Bautzner Landstr. 400, D-01328 Dresden, Germany*

(Dated: 29 August 2022)

In this paper we present a numerical approach to solve the Navier-Stokes equations for arbitrary vessel geometries by combining a Fourier-Spectral method with a direct forcing Immersed Boundary method which allows to consider solid-fluid interactions. The approach is applied to a paradigmatic setup motivated by the precession dynamo experiment currently under construction at Helmholtz- Zentrum Dresden-Rossendorf (*HZDR*). The experiment consists of a fluid filled cylinder rotating about 2 axes which induces a precession driven flow inside the cavity. The cylinder is also equipped with baffles at the end caps with adjustable penetration depth to impact the flow. The numerical details as well as simulation results for the spin-up and precession driven flow in a circular cylinder with additional baffles are presented. The results provide a first confirmation that the use of such baffles in the precession dynamo experiment is a useful way of influencing the flow, allowing more efficient driving without changing the known flow structure too much.

## I. INTRODUCTION

Precession is a well known phenomenon that describes the temporal change of the orientation of the spin axis of rotating objects. In a precessing body filled with a liquid, the fluid interior experiences a volumetric force that directly drives a nontrivial three-dimensional flow. Technical realizations of precessing flows are interesting for their efficiency to mix a passive scalar, which has been realized for example in bladeless mixers to homogenize viscous fluids or used in bioreactors for the growth of micro algae or stem cells[1]. In a spheroidal geometry, the primary flow, directly forced by precession, is called the spin-over mode[2], which is subject to instabilities[3,4] leading to complex three-dimensional velocity structures[5–7]. Such phenomena have been found in experiments and simulations[5,7–9], corroborating the idea that precession is capable of producing strong and complex flow structures in the liquid part of planets[2,10]. For this reason precession is often proposed as an alternative source for powering the geodynamo[11–13] or the ancient lunar dynamo[14–16].

Indeed, simulations in various geometries have shown that precession driven dynamos are possible with a critical magnetic Reynolds number $\mathrm{Rm}^{\mathrm{c}} \sim O(10^3)$[13,17–21], which has motivated the experimental realization of a precession dynamo experiment within the project DRESDYN[22] (Fig. 1). This precession dynamo experiment is currently under construction[23] and will provide a flow of liquid sodium in a cylindrical cavity with a magnetic Reynolds number of up to $\mathrm{Rm}=\Omega_c R^2/\eta \approx 700$ (defined with the achievable angular velocity of the cylinder $\Omega_c = 63\ \mathrm{s}^{-1}$, the radius $R = 1$ m, and the magnetic diffusivity of liquid sodium $\eta = 0.09\,\mathrm{m}^2/\mathrm{s}$). The device represents a considerably enlarged version of the 1970ies experiments conducted by *Gans*[24,25]. These experiments utilized a rather small container so that it had not been feasible to cross the critical magnetic Reynolds number required for the onset of dynamo action. However, it was already possible to observe an amplification of an applied magnetic field by a factor of 3.

Recently, it could be shown by means of kinematic dynamo models combined with scaling properties of a small scale precession water experiment that in the planned precession experiment dynamo action is best possible in a parameter regime where the flow structure is determined by a combination of the nonaxisymmetric directly forced flow and an axisymmetric double roll[26,27]. Such a flow pattern occurs within a narrow regime of precession ratios immediately before the (subcritical) transition into a turbulent state[28]. Although the parameter range at which these models showed dynamos will be achievable in the planned experiments, it is reasonable to think about additional measures, which allow a further impact of the fluid flow. The goal of such modifications is to significantly extend the parameter range with dynamo action, but also to allow dynamos with other characteristic properties, such as other spatial symmetries or dynamic temporal evolution of the magnetic field (like oscillating, bursting or even reversing magnetic fields).

In the present study we realize such an influence by considering radial baffles mounted onto the inner side of the lids of the cylindrical container as originally recommended by *Léorat*[29,30]. Such an installation enhances the azimuthal circulation so that the shear between the bulk flow and the lateral boundaries is reduced. As a result, the transition into the turbulent regime, caused by instabilities in the boundary layers[31] or by an hierarchical emergence of triadic resonances[32], is supposed to be shifted to larger precession ratios, so that a more power-

[a)] Electronic mail: mike.wilbert@ruhr-uni-bochum.de

ful large scale flow, roughly scaling with the precession ratio Po, can be maintained.

The application of internal baffles in a precessing flow has been examined experimentally by[33] in order to suppress turbulence in a precessing system. However, the result was ambiguous, because parameter regimes emerged showing a reduction of energy dissipation as well as regimes with an increased degree of turbulence. Internal baffles are also been used in other dynamo experiments to affect the fluid flow. In the 3 m spherical Couette experiment at Maryland[34], for example, it is planned to attach bended baffles on the inner sphere in order to mimic an increase of the surface roughness, since it was shown numerically that this may allow an onset of dynamo action at experimentally achievable parameters[35].

Baffles were also an essential part of the flow driving in the von Kármán-Sodium (VKS) dynamo[36]. In that experiment a large number of different dynamo states was observed[37], but only if the driving impellers, consisting of a disc and radial baffles attached to this disk, were made of soft iron with a permeability $\mu_r \approx 60$. First mean field models considered idealized distributions of permeability that mimic the shape of the disks and blades and showed that the localized ferromagnetic material causes a reordering of the magnetic eigenmodes with an axisymmetric purely toroidal mode becoming the leading eigenmode[38,39]. But only more sophisticated models were able to explain the exclusive observation of dynamo action in the presence of impellers having high magnetic permeability and the dominant axisymmetric structure[40–42].

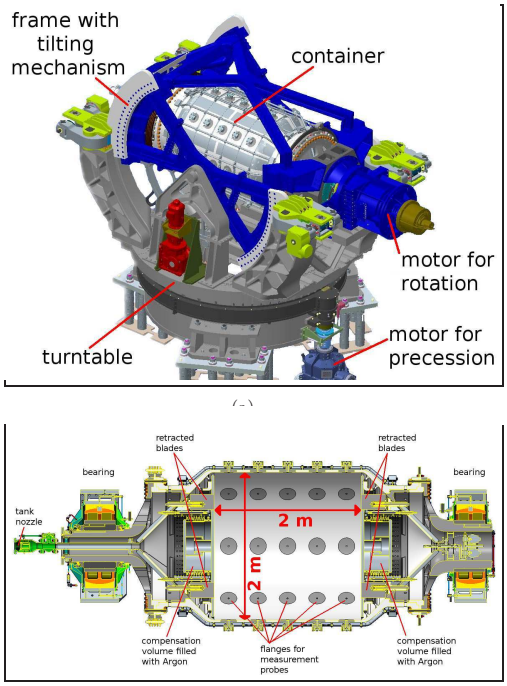


(b)

FIG. 1: Sketch of the precession dynamo experiment consisting of turntable, frame rack, cylindrical container and motors for driving the double rotation. (a) Exterior View. (b) Cross Section.

To perform numerical experiments on the precession driven flow in a cylindrical cavity and especially to study the impact of the baffles on the flow, a new code named *SpecDyn* was developed by the authors which combines the notorious speed of pseudo-spectral methods with the geometrical flexibility of mesh based methods by incorporating a direct forcing Immersed Boundary method.

The paper is organized as follows. First, we give an overview of the applied numerical method, which allows a very fast and well scaling solution of the Navier-Stokes equations due to the highly parallelized algorithm. The interactions between fluid and mechanical structures, i.e. the cylinder walls and the baffles, are calculated by an immersed boundary method with second order accuracy. The reliability of the numerical framework is then demonstrated by simulations of the well known spin-up problem and by comparison with existing numerical solutions of precession driven flows in cylindrical geometry obtained with the finite spectral spectral element code `SEMTEX`[43,44].

Finally, we present extensive numerical studies on precession driven flows in a circular cylinder and discuss the impact of baffles of different lengths on the flow with an emphasis on increasing the flow's potential to drive a self-exciting fluid dynamo.

## II. GOVERNING EQUATIONS

The Problem at hand is to solve for the motion of a Newtonian non-conducting fluid in a precessing vessel. To do so we solve the incompressible Navier-Stokes equations (1) & (2) with no-slip boundary conditions (3).

$$\partial_t \mathbf{u} = \underbrace{\mathbf{u}\times(\nabla\times\mathbf{u})}_{\text{self advection}} + \underbrace{\frac{1}{Re}\Delta\mathbf{u}}_{\text{diffusion}} - \underbrace{\nabla p}_{\text{modified pressure}} + \underbrace{2\,\mathbf{u}\times\boldsymbol{\Omega}}_{\text{Coriolis force}} + \underbrace{\mathbf{r}\times\dot{\boldsymbol{\Omega}}}_{\text{Poincaré force}} \tag{1}$$

$$\nabla\cdot\mathbf{u} = 0 \tag{2}$$

$$\mathbf{u}_{|\Gamma} = 0 \tag{3}$$

The equations are presented in dimensionless form. $\mathbf{U}$ is the fluid velocity, $\Gamma$ represents the boundary of the

fluid domain and $Re$ the Reynolds number defined as $Re = R^2\,\Omega_S\,/\nu$. With cylinder radius $R = 1$ and angular velocity along the axis of symmetry $\Omega_S = 1$. For computational purposes the self advection term is formulated in rotational form. The frame of reference is set so that the bounding vessel is at rest, which makes treating the boundary conditions less complicated. This introduces 3 additional fictitious forces, namely the centrifugal, Coriolis and Poincaré force. $\mathbf{\Omega}$ is the angular velocity of the container, which is time dependent as the precession changes the axis of rotation. For the special case of precession with a right angle between the two rotation axes the angular velocity reads $\mathbf{\Omega} = \mathbf{\Omega}_S + \mathbf{\Omega}_P = \hat{\mathbf{e}}_x + (Po\cos(t)\,\hat{\mathbf{e}}_y + Po\sin(t)\,\hat{\mathbf{e}}_z)$ (c.f. figure 2). The simulation time is normalized to the rotation time of the spin axis which is aligned with the symmetry axis of the cylinder. $Po$ denotes the Poincaré number which is the ratio between the spin and the precession time.
For the incompressible Navier-Stokes equations the pressure acts only as a Lagrangian multiplier to ensure the divergence free condition (2). Since gradient terms only contribute divergence, the actual physical pressure as well as the centrifugal force and the gradient part of the rotational form of the self advection term are combined into the modified pressure gradient $\nabla p$.
Additionally, the plain cylinder bounding geometry can be extended by four baffles at the end caps penetrating into the fluid volume. The depth $d$ of the baffles can be varied smoothly in the DRESDYN experiment up to a maximum of $d_0 = 65\,mm$. Further details on the baffle geometry are given in the caption of figure 2.

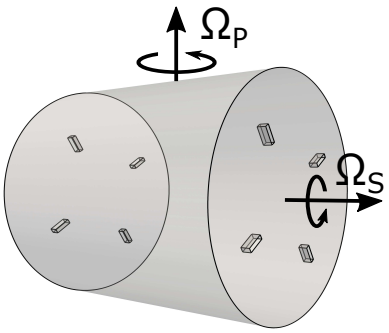


FIG. 2: Schematic drawing of the precessing cylinder with (fully extended) baffles at the end caps. It spins around the symmetry axis with the angular velocity $\mathbf{\Omega}_S$ and is simultaneously in orthogonal precession with angular velocity $\mathbf{\Omega}_P$. The maximum penetration depth of the baffles is $d_0 = 0.065\,R$. They have a width of $w = 0.04\,R$ and their inner and outer radius is $r_i = 0.49\,R$ and $r_o = 0.645\,R$.

The relevant dimensionless numbers representing a scale of the force ratios in the Navier-Stokes equation are the Reynolds number $Re = VL/\nu$ (advection/diffusion), the Ekman number $Ek = \nu/\Omega L^2$ (diffusion/Coriolis force), the Rossby number $Ro = V/\Omega_S L$ (advection/Coriolis force) and the Poincaré number $Po = \Omega_P/\Omega_S$ (Poincaré force/Coriolis force). $\nu$ denotes the kinematic viscosity of the fluid.
With the choice of the characteristic velocity to be that of the cylinder mantle $V = \Omega_S\,R$ and to pick the radius of the cylinder as the characteristic length scale $L = R$, this results in $Ro = 1$ and $Ek = Re^{-1}$.

## III. NUMERICAL METHODS

In this section we introduce the numerical methods implemented in the simulation code *SpecDyn*. First, the basic Fourier pseudo-spectral method is discussed as it is applied. Next we present the details of the immersed boundary method in use which makes it possible to treat the Navier-Stokes equations with no-slip boundary conditions on arbitrarily shaped boundaries and still solve it on a simple Cartesian grid. Eventually, the applied pressure corrector method is discussed, which is necessary after imposing the boundary conditions to ensure the solenoidality of the flow.

### A. Pseudo-Spectral Method

To begin with, we consider the Navier-Stokes equation (1) with periodic boundary conditions and neglect the pressure and consequently the solenoidality of the velocity field. The simulation domain is the cubic box $[-L/2, L/2)^3$ and it is uniformly discretized by $N$ points in each Cartesian coordinate direction. The objective of the Fourier spectral method is to compute spatial derivatives on that grid.
Assuming periodic boundary conditions, the velocity field can be transformed into discrete Fourier space by the Fast Fourier Transform ($FFT$) in a very efficient manner with $\mathcal{O}(Nlog(N))$ operations for each direction[45]. The concept of the method is now to use the fact that spatial derivatives in real space reduce to multiplications of the modes with its wave number in Fourier space. This can be easily shown for the one dimensional case:

$$\begin{aligned}\partial_x u_i &= \left[\partial_x \left(\frac{1}{L}\sum_{j=-N/2}^{N/2-1} \hat{u}_j \exp(ik_j x)\right)\right]_{x=x_i} \\ &= \frac{1}{L}\sum_{j=-N/2}^{N/2-1} (ik_j\hat{u}_j)\exp(ik_j x_i) = \mathcal{DFT}^{-1}\left(ik\hat{u}\right)_{x=x_i}\end{aligned} \tag{4}$$

$u_i$ and $\hat{u}_k$ are the velocity in discrete space and the discrete Fourier modes respectively. $x$ is the space coordinate and $k$ the wave number. The one dimensional

consideration can be trivially extended to three dimensional vector calculus.

The disadvantage of the representation in Fourier space is that multiplications of two spatial dependent quantities in real space become convolutions in Fourier space, which are expensive in terms of computation time ($\mathcal{O}(N^2)$ per dimension) compared to the $FFT$. This case occurs in our special case of the Navier-Stokes equation in the self advection term. The concept of the pseudo-spectral Fourier method is to compute the spatial derivatives of a PDE in Fourier space, calculate its spatial dependent multiplications in real space and transform between those two representations whenever necessary by an $FFT$.

A well known problem inherent to pseudo-spectral methods is the aliasing error[46,47]. That is, a multiplication of two space dependent quantities in real space can produce higher Fourier modes in the result than can be resolved by the discretization. This induces an error especially in the higher modes when the result is transformed to Fourier space where the not resolvable frequencies are falsely interpreted and as a result reflected back into the resolvable spectrum. To minimize or even avoid this error it is common to apply some sort of a low pass filter before and after the multiplications.

A very common method, which is also applied in *SpecDyn*, is the 2/3-rule[48]. Here the Fourier representation of the multipliers are padded with zeros in the upper third of the spectrum. As a result their product contains the reflected modes in the upper third and the frequencies of interest are purely separated in the rest of the spectrum. The erroneous modes can therefore be easily removed by again padding the upper third of the results spectrum by zeros. The 2/3-method thus completely removes the aliasing error at the expense of a decrease in resolution.

After the r.h.s. of the Navier-Stokes equation (without the pressure gradient) is evaluated the remaining problem is to solve an ordinary differential equation in time. For this purpose we use the strong stability preserving Runge-Kutta scheme of convergence order 3 (SSPRK3)[49].

Since the Runge-Kutta scheme in use is an explicit method its stability is restricted by the size of the time step $\Delta t$. For the Navier-Stokes equation the advection as well as the diffusion term impose a cfl condition respectively:

$$\Delta t \leq C \, \frac{\Delta x}{u_{max}} \tag{5}$$

$$\Delta t \leq C \, Re \, (\Delta x)^2 \tag{6}$$

$\Delta x$ denotes the distance between neighbored grid points, $u_{max}$ is the maximum value of the velocity and $C$ is the cfl number which is equal to 1 for the SSPRK3 scheme[50]. The condition arising from the diffusion term (6) is far more restrictive when the spatial resolution is increased. Hence it is common practice to treat the diffusion term by an implicit scheme.

Since the diffusion equation can be easily solved in Fourier space we make the following ansatz to treat the diffusion analytically:

$$\partial_t \mathbf{u}_k(t) =: \tilde{\mathbf{u}}_k(t) \exp\left(-\frac{k^2}{Re} t\right) \tag{7}$$

$\mathbf{u}_k$ denotes the velocity in discrete Fourier space associated with the wavenumber $k$.

Inserting this into the Navier-Stokes equation (1) we receive a new PDE for $\tilde{\mathbf{u}}_k$

$$\partial_t \tilde{\mathbf{u}}_k = RHS(\mathbf{u}_k, t) \exp\left(+\frac{k^2}{Re} t\right) \tag{8}$$

$RHS$ stands for all r.h.s. terms of the Navier-Stokes equation excluding the diffusion term.

So the process is to integrate (8) to advance the auxiliary velocity $\tilde{\mathbf{u}}$ in time and thereafter compute the the actual velocity $\mathbf{u}$ from (7). This is done in each Runge-Kutta sub-step.

So far we have ignored the pressure gradient in the Navier-Stokes equation. At this point we describe the pressure correction scheme proposed by Chorin[51] & Temam[52] sufficient if no boundary conditions other than periodic boundary conditions are imposed in a pseudo-spectral code. The method is an equation splitting scheme which we will deduce heuristically by means of the simple explicit Euler scheme. First we expand the Euler step by an auxiliary velocity $\bar{\mathbf{u}}$

$$\frac{\mathbf{u}^{n+1} - \bar{\mathbf{u}}^{n+1} + \bar{\mathbf{u}}^{n+1} - \mathbf{u}^n}{\Delta t} = \underline{RHS}(\mathbf{u}^n, t_n) - \nabla p^{n+1} \tag{9}$$

$\underline{RHS}$ denotes the r.h.s. of the Navier-Stokes equation excluding the pressure gradient and the superscript $n$ refers to the discrete time value $t_n = n\Delta t$.

The Euler step (9) can now be split into two separate equations. First the time integration is performed without the pressure gradient and in the second step the divergence of the auxiliary velocity $\bar{\mathbf{u}}$ is removed.

$$\frac{\bar{\mathbf{u}}^{n+1} - \mathbf{u}^n}{\Delta t} = \underline{RHS}(\mathbf{u}^n, t_n) \tag{10}$$

$$\frac{\mathbf{u}^{n+1} - \bar{\mathbf{u}}^{n+1}}{\Delta t} = -\nabla p^{n+1} \tag{11}$$

The pressure can be calculated by taking the divergence of (11) and using the solenoidality of the final velocity $\mathbf{u}^{n+1}$.

$$\frac{\nabla \bar{\mathbf{u}}^{n+1}}{\Delta t} = \Delta p^{n+1} \tag{12}$$

Solving this Poisson equation takes usually up a great amount of computing time e.g. in a finite difference code. However, (12) can be simply reversed in Fourier space. (11) & (12) can consequently be combined to a single projection step in Fourier space

$$\mathbf{u}^{n+1} = \mathcal{P}\bar{\mathbf{u}}^{n+1} := \bar{\mathbf{u}}^{n+1} - \mathbf{k} \cdot \frac{\mathbf{k} \cdot \bar{\mathbf{u}}^{n+1}}{|\mathbf{k}|^2} \tag{13}$$

This is also known as *Leray projection*[53].
In a later section we will cover an advanced pressure correction method to consistently combine the solenoidality condition with the no-slip boundary condition under consideration of a tolerable splitting error.

### B. Immersed Boundary Method

The Immersed Boundary Method (*IBM*) was originally proposed by Peskin[54] in the context of fluid-structure interactions in the field of biological fluid dynamics. This particular problem involves elastically moving boundaries and the fluid as well as the boundaries produce feedback forces on one another. The original method is based on the idea to describe the boundary of a Lagrangian mesh but to treat the fluid on an Eulerian grid and change between those two views by means of a discrete Dirac function. This was the basis for the development of a range of *IBM* methods in the context of elastic boundary flows[55].
The advantage of the IBM to treat arbitrary bounding geometries but restrict the main computations to a simple (e.g. Cartesian) grid is also appealing for fluid simulations with solid boundaries. The *IBM* of Peskin was adapted by Goldstein et al.[56,57] to treat rigid boundaries. The method inherits the concept that the fluid solely recognizes the solid boundary by forces acting on the flow. Hence they computed the fluid on a Cartesian grid with an additional force representing the boundary which was modeled by

$$\mathbf{F}_{IB} = \alpha \int_0^t [\mathbf{U} - \mathbf{V}_{IB}]\,\mathrm{d}t + \beta\,[\mathbf{U} - \mathbf{V}_{IB}] \tag{14}$$

with two adjustable negative parameters $\alpha$ and $\beta$. $\mathbf{V}_{IB}$ denotes the velocity imposed on the boundary and $\mathbf{U}$ the actual velocity field without a boundary condition. The force then is only applied to grid points near the boundaries and consequently smoothed out. Neglecting all other forces in the Navier-Stokes equation the IB forcing term results in a damped harmonic oscillation in the difference between the real and the demanded velocity on the boundary[56]. Goldstein et al. used a pseudo-spectral method and realized the smoothing by a sharp Gauss distribution to simulate the flow over a riblet covered surface, the flow over an accelerated cylinder and other problems[56,57]. Saiki and Biringen[58] used the same forcing in a finite-difference code with a different interpolation procedure for the smoothing. Peskin and Lai[59] used the approach by Saiki and Biringen but with a spectral method and slightly moving boundary points.
The two main drawbacks of this method are on the one hand that by the smoothing the boundary is not sharply represented which reduces the accuracy[60] and on the other hand the two parameters inherent in the forcing have to be determined by numerical experiments and can cause instabilities and therefore restrict the time step[60,61].
Another feedback forcing IB method was proposed by Arquis & Caltagirone[62] by treating the solid as porous media and hence introduce an additional force term which models the Darcy drag[63]. This penalization term comes with the permeability $\eta$ as a free parameter. The penalized version of the equation converges to the original problem of the Navier-Stokes equation with no-slip boundary conditions with an error of order $\mathcal{O}(\eta^{1/2})$. Therefore the penalization parameter $\eta$ is chosen usually as small as possible. Unfortunately the drag term introduces a time scale which has to be resolved and the stability is only ensured for $\eta \geq \Delta t/2$ [64]. This restriction on the stability can be circumvented by treating the drag term implicit in the time stepping[64]. Nevertheless, a temporal not well resolved drag force just sets the solid velocity to zero which correlates to the zeroth order direct forcing IB method discussed by Fadlun et al.[65] Another disadvantage of the method is that the drag term produces a boundary layer inside the solid[63] and hence smears out the border. The method can formally be reduced to the forcing of Goldstein et at. by setting $\alpha = 0$ and $\beta = 1/\eta$ [61]. The method was applied successfully to various phenomena as the flow inside an IC piston[66], insect flight[67] and magnetohydrodynamic flows[68–70].
An alternative to the above-mentioned IB methods is the direct forcing approach introduced by Mohd-Yusof[71]. In this method the forcing is directly applied to the flow to ensure the boundary conditions and therefore neither introduces a stability criterion on the time step nor is there any free parameter to be chosen[60]. The method was shortly after successfully applied to the flow inside a motored piston[65,72] in an LES simulation.
For the explicit Euler time stepping the force $\mathbf{F}_{IB}$ can be formally defined as follows

$$\frac{\mathbf{V} - \mathbf{u}^n}{\Delta t} - RHS =: \mathbf{F}_{IB} \tag{15}$$

$\mathbf{V}$ denotes the imposed solid velocity and $RHS$ incorporates all r.h.s. terms of the Navier-Stokes equation. The IB force is only applied to the grid nodes coinciding with the boundary and the only effect of this force is to impose the boundary condition on those nodes. In practice the force is rarely computed and instead the velocity is directly set to some desired value at the boundary[60]. It should be mentioned that the forcing in this method acts as a Lagrangian multiplier to ensure the boundary conditions in the same way as the pressure gradient simply guarantees the incompressibility.
Since the boundary points are very unlikely to coincide with the computational grid an interpolation procedure is required. Fadlun et al.[65] have presented three different kinds of possible interpolation procedures, which they found to be zeroth, first and second order accurate respectively. First we will discuss these in one spatial dimension with the aid of figure 3.

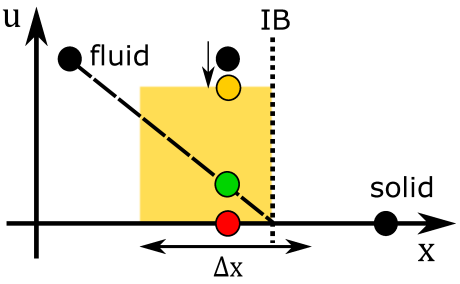


FIG. 3: Schematic drawing of the three direct forcing interpolation methods proposed by Fadlun et al.
red: zeroth order, yellow: first order, green: second order

- $0^{th}$ order: The velocity on the nodes closest to the boundary is simply set to the demanded boundary value (red circle in the figure)
- $1^{st}$ order: The velocity on the nodes closest to the boundary is the weighted average between its own velocity computed without the boundaries and the solid velocity. For the weighting the cell around the specific node is considered and the weighting coefficients are computed dependent on how far the cell extends into the solid. In three dimensions this becomes a volume weighting. This method can be easily implemented with a Monte-Carlo approach[73]. (yellow circle in the figure)
- $2^{nd}$ order: The velocity is interpolated on all nodes in the fluid adjacent to the solid. The interpolation is performed linearly between the closest fluid node and the exact location of the boundary (green circle in the figure)

We use the second order approach, since in a pseudo-spectral code the error of the Fourier interpolation scales with the smoothness of the fields[46], although the first order approach is easier to implement for complex geometries. We will classify points on the grid as fluid and solid nodes. Additionally we define IB nodes as all fluid nodes with at least one neighbored solid node.
Another point to consider is how to represent the boundaries. For simple 2D geometries a Lagrangian grid can be used and the nodes on that grid can then e.g. be interpolated by a b-spline[74]. Iaccarino & Verzicco[60] discussed the use of meshes generated by CAD programs and Sotiropoulos et al.[75–78] based a series of papers on the idea of combining the direct forcing *IBM* method with triangular meshes usually used for finite element simulations. We also employ this approach and use the parametric 3D CAD modeler *FreeCAD*[79] to construct the models of the fluid vessel and utilize the finite element mesh generator *gmesh*[80] to transform the model into a triangular mesh. Those meshes saved in the .ply format (*Stanford Triangle Format*) can then directly be read by *SpecDyn*.
After the triangular grid is imported to the simulation program a routine is required to decide which of the Cartesian grid points are located inside the solid and which in the fluid. To do so we act on the suggestion by Sotiropoulos et al.[78] to employ a ray-tracing algorithm. The method originally used by Sotiropoulos et al.[81] was found not to be sufficient for our purposes and created errors by rays slipping through gaps between the triangles due to finite floating point precision. We therefore choose the 'watertight' ray-tracing algorithm presented by Woop et al.[82]
When we expand our previous considerations to three dimensions the question naturally arises in which direction the linear interpolation is carried out. Fadlun et al.[65] originally used an arbitrary direction along the Cartesian coordinate lines. On the other hand Balaras[74] suggested to perform the interpolation normal to the boundary. In the latter procedure different realizations have to be considered since here no fluid node is usually reached by the normal close to the surface. Therefore some interpolation of the surrounding fluid nodes has to be performed. Additionally some of the nodes in the fluid are marked as IB nodes, which can not be used for the interpolation. The latter also led us to discard the interpolation along the normal after some numerical testing. In very concave areas of the bounding surface most of the nodes in the fluid are actually IB nodes. Therefore extending the normal until enough fluid nodes surround the tip of the normal, as done by Balaras[74] and later by Sotiropoulos et al., is in some cases not feasible since the distance from the surface to the considered point is too large (see figure 4b). In fact, Balaras and Sotiropoulos et al.[75–78] mostly considered convex shaped boundaries. Finally we decided to choose the concept of Fadlun et al.
In *SpecDyn* for every IB node all 6 neighboring cells are perused. If one is a fluid node and the neighbor on the other side of the IB cell on the same coordinate line is a solid node, this line is chosen to perform the interpolation on (see figure 4a). If the condition is not fulfilled for all 3 directions, then the nodes reachable from the IB node by going a node distance $\Delta x$ in two coordinate directions respectively are considered. Again, if one of these nodes is a fluid node and its counterpart on the other side of the IB node is a solid node, it is chosen as the interpolation line (see figure 4b).

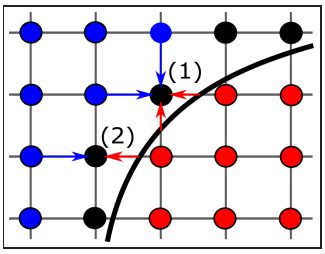


(a) Interpolation for a convex surface. The velocity on the IB node (1) can be interpolated in two different directions (horizontally and vertically). Whereas the velocity on IB node (2) can only be computed by interpolation in the horizontal direction.

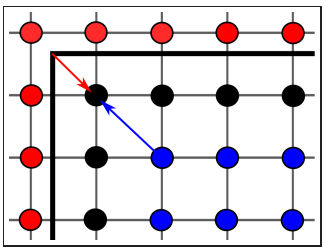

(b) For the concave corner an interpolation along the surface normal would not be possible since all nodes on that normal in the fluid are marked as IB nodes. For the same reason an interpolation along a coordinate line is not feasible. For those cases the line connecting the diagonal neighbors of the IB node is chosen as the interpolation path.

FIG. 4: Schematic drawing presenting the linear interpolation of the immersed boundary to the IB nodes in two dimensions for a convex surface (a) and a concave corner (b). Shown are the three different types of nodes: fluid (blue), solid (red) and IB (black). The boundary is represented by a thick black line.

If also this case is false, nodes reached from the IB nodes by going one node distance $\Delta x$ in all three coordinate directions respectively is considered with the same procedure as for the other cases mentioned above. The solid nodes are set in every case to the desired value.
The direct forcing IBM has been successfully applied to the flow through a bileaflet mechanical heart valve[77], in a nuclear rod-bundle[83] and to the flow past an in-line oscillating cylinder[84], just to name a few applications.

### C. Pressure Predictor Method

Both the pressure and the IB force act as Lagrangian multipliers to impose the incompressibility (2) and the no-slip boundary condition (3) respectively. Unfortunately the operations of imposing each condition do not commute and therefore by enforcing one of the two we introduce an inaccuracy in the other. If we take for instance the pressure projection scheme by Chorin & Temam discussed in section III A and enforce the boundary condition between the time step (10) and the projection step (11) this introduces an error in the velocity $\epsilon_u \sim \mathcal{O}(\Delta t)$ and an error in the pressure $\epsilon_p \sim \mathcal{O}(\Delta t^{1/2})$[85]. A class which applies oneself to this issue are the so called pressure-correction schemes[86].
Van Kahn[87] developed a scheme based on the idea by Goda[88] in which first the divergence of the velocity is approximately removed by applying the pressure gradient of the previous time step before enforcing the boundary condition and thereafter projecting it to divergence free space. This scheme will be denoted as the incremental pressure-correction scheme. It has improved convergence properties compared to the projection scheme by Chorin & Temam and the errors in velocity and pressure are of order $\epsilon_u \sim \mathcal{O}(\Delta t^2)$ and $\epsilon_p \sim \mathcal{O}(\Delta t)$.[86] The scheme can be heuristically derived as follows for the simple explicit Euler time stepping by expanding it by the pressure gradient of the last time step $\nabla p^n$:

$$\begin{aligned}&\frac{\mathbf{u}^{n+1}-\bar{\mathbf{u}}^{n+1}+\bar{\mathbf{u}}^{n+1}-\mathbf{u}^n}{\Delta t}\\&=\underline{RHS}(\mathbf{u}^n,t_n)-\nabla p^{n+1}+\nabla\left(p^n-p^n\right)\end{aligned} \tag{16}$$

and splitting this time step into

$$\frac{\bar{\mathbf{u}}^{n+1}-\mathbf{u}^n}{\Delta t}=\underline{RHS}(\mathbf{u}^n,t_n)-\nabla p^n \tag{17}$$

$$\frac{\mathbf{u}^{n+1}-\bar{\mathbf{u}}^{n+1}}{\Delta t}=-\nabla q^n,\quad q^n:=p^{n+1}-p^n \tag{18}$$

The boundary condition is then enforced in between those two steps. The auxiliary field $q^n$ can, like in the Chorin & Temam method, be computed by taking the divergence of equation (18) and utilizing the solenoidality of the final velocity $\mathbf{u}^{n+1}$.
Although the incremental pressure-correction scheme is an improvement over the Chorin & Temam projection method it is only converging linearly in the pressure. This is caused by a numerical boundary layer produced by the scheme[86]. Timmermans et al.[89] further improved the method to reduce the error in the pressure to $\epsilon_p \sim \mathcal{O}(\Delta t^{3/2})$ [90]. The critical point can be seen if we extract the diffusion term from $\underline{RHS}^n$. Since we treat the diffusion term analytically the first step in the incremental pressure-correction scheme (17) can be written as

$$\frac{\bar{\mathbf{u}}^{n+1}-\mathbf{u}^n}{\Delta t}=\underline{\underline{RHS}}(\mathbf{u}^n,t_n)+\frac{1}{Re}\Delta\bar{\mathbf{u}}^{n+1}-\nabla p^n \tag{19}$$

Notice that in this step the diffusion is carried out with the auxiliary field $\tilde{\mathbf{u}}^{n+1}$ instead of the actual velocity $\mathbf{u}^{n+1}$. This discrepancy can be rectified by extending the time step before the splitting (16) by the undesired diffusion term $(1/Re\ \Delta\bar{\mathbf{u}}^{n+1})$.

$$\frac{\mathbf{u}^{n+1}-\bar{\mathbf{u}}^{n+1}+\bar{\mathbf{u}}^{n+1}-\mathbf{u}^{n}}{\Delta t}=\underline{\underline{RHS}}(\mathbf{u}^{n},t_n)+\frac{1}{Re}\Delta\mathbf{u}^{n+1}$$
$$-\nabla p^{n+1}+\nabla\left(p^{n}-p^{n}\right)+\frac{1}{Re}\Delta\left(\bar{\mathbf{u}}^{n+1}-\bar{\mathbf{u}}^{n+1}\right) \tag{20}$$

$\underline{\underline{RHS}}$ denotes the r.h.s. of the Navier-Stokes equation without the pressure gradient and the diffusion term. Notice that in this form the diffusion is executed with the appropriate velocity $\mathbf{u}^{n+1}$ and the step can be splitted as follows

$$\frac{\bar{\mathbf{u}}^{n+1}-\mathbf{u}^{n}}{\Delta t}=\underline{\underline{RHS}}(\mathbf{u}^{n},t_n)+\frac{1}{Re}\Delta\bar{\mathbf{u}}^{n+1}-\nabla p^{n} \tag{21}$$
$$\frac{\mathbf{u}^{n+1}-\bar{\mathbf{u}}^{n+1}}{\Delta t}=-\nabla(p^{n+1}-p^{n})+\frac{1}{Re}\Delta\left(\mathbf{u}^{n+1}-\bar{\mathbf{u}}^{n+1}\right) \tag{22}$$

Next we consider the vector identity $\Delta\mathbf{v}=\nabla(\nabla\cdot\mathbf{v})-\nabla\times(\nabla\times\mathbf{v})$, which represents a Helmholtz decomposition for $\Delta\mathbf{v}$. Since $\mathbf{u}^{n+1}$ is generated from $\tilde{\mathbf{u}}^{n+1}$ by the projection to the divergence free space $\Delta\mathbf{u}^{n+1}$ and $\Delta\tilde{\mathbf{u}}^{n+1}$ only differ by their divergence. So the second part in the vector identity is equal for both quantities and the first part vanishes for $\mathbf{u}^{n+1}$ for it is divergence free. Therefore the projection step (22) can also be written as

$$\frac{\mathbf{u}^{n+1}-\bar{\mathbf{u}}^{n+1}}{\Delta t}=\nabla\Phi^{n},\ \Phi^{n}:=p^{n+1}-p^{n}+\frac{1}{Re}\nabla\cdot\bar{\mathbf{u}}^{n+1} \tag{23}$$

The auxiliary field $\Phi^n$ can be obtained as before by taking the divergence of (23) and this method will be denoted as the rotational incremental pressure-correction scheme. It overcomes the issue of the incremental pressure-correction scheme and only produces an error at the boundary in the tangential direction[89]. This scheme is applied in the code *SpecDyn*.

## IV. PARALLELIZATION & CODE PERFORMANCE

To obtain the necessary resolution in three dimensions with feasible computing time a massive parallelization of the code is mandatory to perform on modern super computers.

The only global operation in our pseudo-spectral code is the *FFT*. There exist several libraries to perform parallel *FFT*s such as the *P3DFFT*[91], *2DECOMP&FFT*[92] and the *PFFT*[93], which all in general follow the same procedure. The three dimensional discrete domain of interest is divided among a Cartesian processor grid either in one (slab decomposition) or two dimensions (pencil decomposition). Thus in every case at least one dimension is fully available on each process. Along this direct a regular 1D FFT can be performed. To cover the other directions, the processor grid is then transposed so that another directions is fully available on each process. This sequence of 1D *FFT*s and processor grid transpositions is performed until all directions are transformed to discrete Fourier space. For a 3D pencil decomposition this makes three 1D *FFT*s and two processor grid transpositions. Our simulations are carried out in the reference frame of the cylinder but the experimental data is obtained in the reference frame of the turntable. Since the baffles make the cylindrical vessel no more rotational symmetric it is necessary to rotate the velocity field for the transformation to maintain the right angle of the vessel in the turntable frame of reference. This is especially required to generate time averaged fields. For that purpose we use the method proposed by Larkin et al.[94] who utilize the Fourier shift theorem to perform the rotation by three shear transforms. To apply this method one has to be able to perform 1D *FFT*s in arbitrary directions. This feature is, to the best of the authors knowledge, not supported by the available parallel C++/FORTRAN *FFT* libraries. Hence, we implemented the parallel *FFT* in slab decomposition by ourselves after the procedure proposed by Mortensen et al.[95].

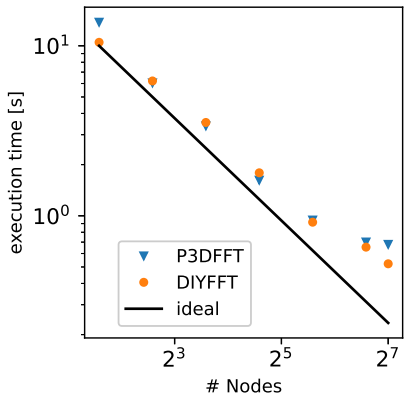


FIG. 5: *DIYFFT vs. P3DFFT*. Scaling of 100 real-to-complex/complex-to-real FFTs with pencil decomposition on a grid of size $512^3$. The computation was performed on the *JUWELS* CPU cluster with 48 CPUs per node. The 1D *FFT*s were carried out by the *FFTW* library for both cases.

They realize the parallelization with the aid of the Message Passing Interface (MPI)[96] and deploy MPI datatypes and the MPI API-routine MPI_all2allw to provide

an efficient and easy to implement parallel *FFT*. Our implementation will be denoted as *DIYFFT* and we utilize the widely used *FFTW* library[97] to perform the 1D *FFT*s. The scaling of our parallel *FFT* implementation compared to the *P3DFFT* is shown in figure 5 and the performance of the complete code *SpecDyn* is depicted in figure 6. All computations carried out with the code *SpecDyn* presented in this paper were performed on the JUWELS CPU cluster module located at Forschungszentrum Jülich in Germany.[98]

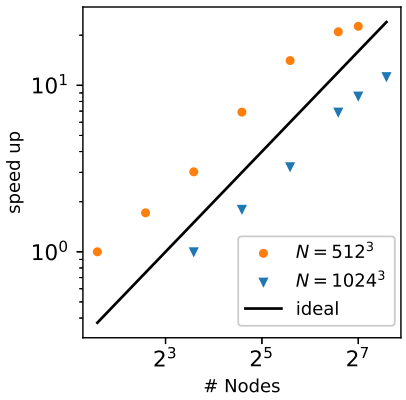


FIG. 6: Scaling of *SpecDyn* for 100 time steps on a grid of size $512^3$ and $1024^3$. The computation was performed on the *JUWELS* CPU cluster with 48 CPUs per node. The speed up is normalized to 3 nodes for $N = 512^3$ and to 12 nodes for $N = 1024^3$.

## V. RESULTS AND DISCUSSION

In this section we present numerical experiments concerning the DRESDYN dynamo experiment. The geometrical setup is given in section II.
We investigate the influence of the baffles on the flow in two different setups: First the spin-up is studied, i.e. the abrupt increase of the angular velocity of the container. Especially the time needed by the spin-up process is of interest for the real world experiment. Next we extend the setup so that the cylinder additionally rotates about an axis perpendicular to the symmetry axis. This precession driven flow and its potential as a source for dynamo action is the main object of interest in this paper.

### A. Spin-Up

In this section we discuss the impact of baffles at the end caps of a circular cylinder on the spin-up flow.

Consider a fluid contained in a cylinder, both rigidly rotating about the symmetry axis of the cylinder with angular velocity $\Omega$. Then suddenly the velocity of the vessel is increased by an amount $\Delta\Omega$. Spin-up refers to the adjustment of the fluid flow to the new boundary condition and its transition to a solid body rotation identical to that of the cylinder.

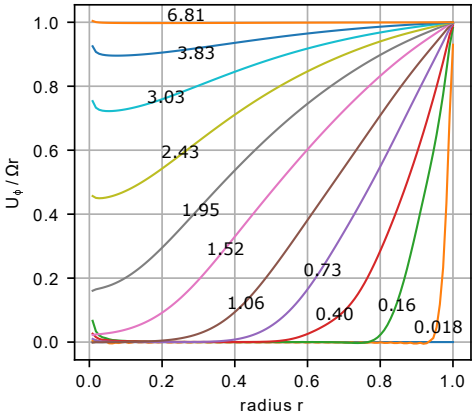


FIG. 7: Profile of the azimuthal velocity divided by the solid body rotation in the meridional plane in the plain cylinder geometry at $Re = 6400$. The numbers on the lines denote the respective time measured in the unit of the spin-up time $t_E$.

The spin-up is a widely studied problem[99–101].
A milestone in the theory was the paper by Greenspan & Howard[102] who developed a linear theory for small Ekman $Ek$ and Rossby number $Ro$ flows between two similarly rotating infinitely extended disks. Because of the relation $Ek = Re^{-1}$ due to the choice of the characteristic scales, we will present our results in terms of $Re$, whereas the general spin-up theory uses $Ek$ as a measure of scale. The process behind the linear spin-up can be roughly sketched as follows: The higher angular velocity at the disks forms a shear layer which after a short time evolves into an Ekman boundary layer due to viscous effects. In this layer the fluid is pushed radially outwards and has to be compensated for the sake of incompressibility by fluid flowing from the inner region to the Ekman layer. The same argument of mass-flux conservation leads to the formation of a circular motion between the disks and the bulk transporting fluid from the practically inviscid inner region into the Ekman layer, where its angular velocity is increased.[103] This process is also known as Ekman pumping. The time scale for the spin-up was proposed by Greenspan & Howard to $t_E = Ek^{-1/2}\Omega^{-1}$, which is much shorter than

the spin-up solely due to diffusion of the boundary layer ($\sim Ek^{-1}$).[102]

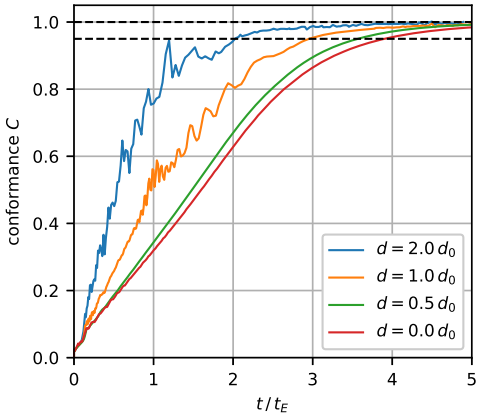


FIG. 8: Conformance $C$ of the azimuthal velocity with the solid body rotation at $Re = 6400$ for different baffle depths $d$. The dashed lines mark the values of 0.95 and 1.

If the fluid is enclosed in a cylindrical vessel, the no-slip boundary condition forces Stewartson layers to form at the cylinder mantle. Although they are not of relevance for the linear spin-up[99], they are essential to the non-linear model developed by Wedemeyer[104] for $Ro = 1$. This model was later modified by Venezian[105] to treat Rossby numbers in the range of $0 < Ro \leq 1$. The new feature introduced in the case of non-linear spin-up is the Stewartson layer propagating into the fluid towards the symmetry axis. This shear layer divides the flow into two regions. The flow between that shear layer and the cylinder mantle is spun-up whereas the angular velocity in the inner region is unaffected. This mechanism takes a few spin-up times to fully spin-up the fluid.[99] In this paper we invest the non-linear spin-up from rest ($Ro = 1$). The theoretical predicted mechanism is also observed in our numerical investigations as depicted in figure 7

To study the impact of the baffles on the spin-up we consider the azimuthal velocity $U_\phi$ divided by the solid body rotation $\Omega\, r$ on a line in the equatorial plane of the cylinder reaching from the center radially outward to the wall. To quantify the adaption of the flow to the solid body rotation we integrate over this line, obtaining $C(t) = \int_0^1 U_\phi(t)\,/\,\Omega r\,\mathrm{d}r$ as a measure of the conformance of the flow. The temporal development of the flow is depicted in figure 8 for $Re = 6400$ and different baffle depths.

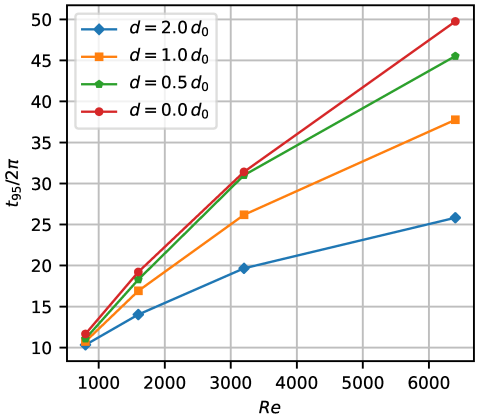


FIG. 9: Number of rotations to reach 95% of the solid body rotation for different Reynolds numbers and blade depths.

Since the spin-up is adopted asymptotically we considered the time $t_{95}$ when the confirmation $C$ reaches a value of 95%. $t_{95}$ was measured for different Reynolds numbers $Re$ and four different blade depth $d$. The result of this examination is presented in figure 9.

First of all it is to notice that the theoretical predicted scale of the spin-up time proportional to $Ek^{-1/2}$ for the plain cylinder geometry is not strictly presented by our results. This lies in the fact that the condition of low diffusion relative to the Coriolis force ($Ek \ll 1$ or $Re \gg 1$ for our setup) is not given for the presented range of $Re$ values. Whereas in the case of dominant diffusion ($Re \approx 1$), the spin-up time is given as the diffusion time $Re$. The presented results are based on $Re$ values lying in between those two assumptions.

Further the immersion of the baffles drastically reduces the spin-up time, although the baffles produce additional oscillations. These are, however, almost completely damped as $t_{95}$ is reached. The influence of the baffles extended to half the maximum penetration depths $d_0$ is only small. However, the extension to full or double the maximum penetration depths has a perceptible influence on the spin-up time. As for $Re = 6400$ it reduces $t_{95}$ to nearly 75% for baffle length $d_0$ and to even nearly 50% for baffles lengths of $2\,d_0$. As the Reynolds number increases, the influence of the baffles becomes more dominant. This trend could lead to an even greater reduction of the spin-up time in the real world experiment by fully extended baffles, since in it values of $Re$ will be reachable orders of magnitude greater than those which were feasible to treat by our simulations.

### B. Precession Driven Flow

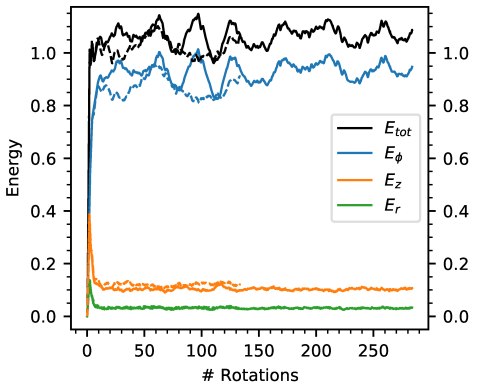


FIG. 10: Kinetic energy development over time with plain cylinder geometry for $Po = 0.1$ and $Re = 6500$. Shown are the total kinetic energy $E_{tot}$ as well as the components in the cylindrical coordinate directions $(E_r, E_\phi, E_z)$. The solid lines refer to results from *SpecDyn* whereas the dotted lines belong to simulations produced by *SEMTEX*.

In this section we present results concerning precession driven flows in a circular cylinder and the impact of baffles at the end caps on the flow. The parameters to be varied to influence the flow are particular the Reynolds number $Re$, the Poincaré number $Po$ and the overall geometry of the vessel. The aspect ratio of the cylindrical container in the real world experiment is fixed to $\Gamma = H/R = 2$ (height equals diameter), which is close to $\Gamma = 1.98982$, the first resonance of the primary response to precesional forcing[106]. A variation of the geometry only arises from different length of the baffles at the end caps reaching into the fluid. Here we restricted the baffle lengths to 0.5, 1, 1.5 and 2 times the maximum penetration lengths $d_0$ concerning the *DRESDYN* experiment.

In precession experiments with plain cylindrical vessels the fluid traverses laminar, non-linear and turbulent behavior with increasing forcing in terms of $Po$. The critical thresholds for these transitions depend on the Reynolds number $Re$ in a nontrivial manner although experiments suggest that for sufficiently large $Re$ an asymptotic behavior occurs[27].

As the focus of this study lies on flows suitable for the onset of dynamo action, the laminar phase is of minor interest. Therefore a sufficiently high $Re$ has to be chosen. At the same time the thickness of the boundary layer, that has to be resolved in the numerical simulations, decreases with the Reynolds number as $\sim Re^{-1/243}$. As a compromise we choose a Reynolds number of $Re = 6500$ for all of the simulations presented in the remainder of this paper. At this value the laminar regime is already overcome and the boundary layer is resolved with 2 grid nodes for the chosen resolution of $N = 256$ in each coordinate direction.

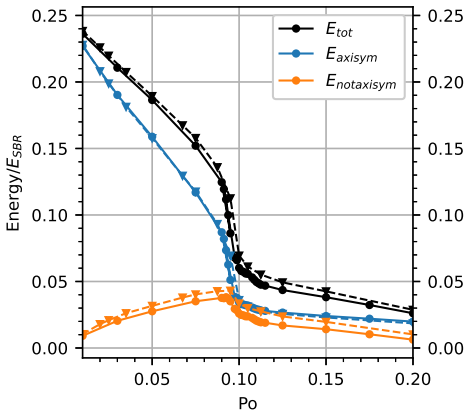


FIG. 11: Total energy as a fraction of the energy of a solid body rotation partitioned into axisymmetric and non-axisymmetric energy as a function of the Poincaré number $Po$. The solid lines present the results produced by *SpecDyn* and the dashed lines refer to those computed by *SEMTEX*.

#### 1. Validation of SpecDyn

Our results obtained with *SpecDyn* are in good agreement with the results obtained previously with the code *SEMTEX* as presented e.g. in Pizzi et al.[43]. *SEMTEX* is a spectral element code which was already successfully applied to study precession driven flows. As a result of its numerical procedures it is solely capable to treat plain cylindrical vessels so that we restrict the comparison to a setup without baffles. We initialize the fluid with zero velocity in the reference frame of the cylinder mantle, i.e. with two superimposed solid body rotations of ratio $Po$ in the laboratory frame.

After an initial growth phase the energy goes into saturation. Figure 10 depicts this process for a Poincaré number of $Po = 0.1$ and compares our results with those produced with *SEMTEX* The energy components as well as the strength and frequency of the fluctuations take on comparable values.

We now consider the time-averaged energy partitioned into its axialsymmetric and non-axisymmetric fraction. The energy dependence on $Po$ is depicted in Fig.

11 for the plain cylinder and again compared to the computations produced by *SEMTEX*. In the region just below $Po \approx 0.1$ we observe a change from a linear trend to a rapid drop in the axialsymmetric energy as well as a maximum in the non-axisymmetric energy. In this region it is known from previous studies[27,43] that the forced mode breaks down and feeds an intermediate double roll structure as well as higher modes. For even higher Poincaré numbers the energy components again take on a nearly linear dependence on $Po$. The energy components produced by both codes are in good agreement although the non-axisymmetric energies differ by a small offset.

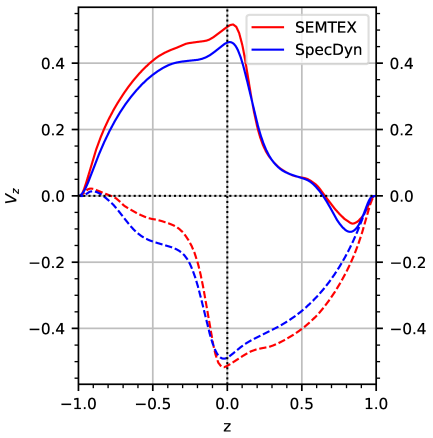


FIG. 12: Time averaged axial velocity $V_z$ along the axial line which passes through the maximum (solid line)/ minimum (dashed line) of the axial velocity in the centered equatorial plane. The frame of reference is is that of the turntable and the velocity is compared to that produced by SEMTEX.

A more detailed comparison of the structure of the axial flow component is given in figure 12. Here the axial velocity is plotted over two lines along the axial direction. The position of the lines is chosen so that they pass through the point of maximum/minimum axial velocity respectively in the equatorial plane centered in the cylinder. The dominating feature to observe here is the forced mode produced by the precession. Again we compare our results with those produced both the code. The overall behavior of both plots is in good agreement although the result produced by *SpecDyn* exhibits mostly slightly smaller values and the velocity profile features little more asymmetry.

### 2. *Impact of baffles*

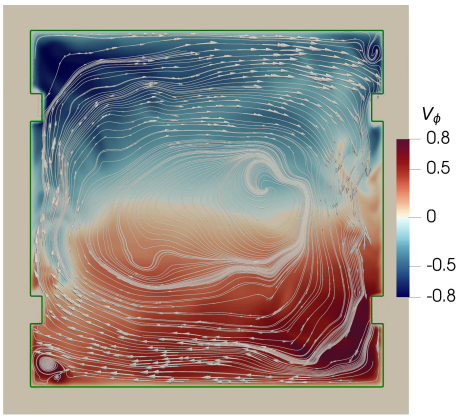


FIG. 13: Streamlines in meridional plane. Baffle length $= 1 \times d_0$, time $= 283 \times 2\pi$, $\epsilon = 0.1$. The azimuthal velocity $V_\phi$ is color coded whereas the the streamlines relate to the velocity projected to the meridional plane. The green lines indicate the solid boundary.

In the following we discuss and analyze the results obtained when adding baffles with various height. For these results only data from simulations with *SpecDyn* are used. We consider the time averaged velocity field in the frame of reference of the turntable over the interval of 153 to 183 rotations around the axis of symmetry. In that time regime we can be sure that the fluid flow is already saturated. The main qualitative result from these simulations is that adding baffles does not dramatically change the general behavior of the flow.
The most dominant mode occurring is the forced mode, a non-axisymmetric mode forced by the precession ($\sim cos(\phi)$). This mode enforces a recirculation of the fluid as a results of the permanent change of the rotation axis. This mode can be seen in figure 13. The figure also depicts the flow around the edges of the baffles and the forming of eddies in the edges of the cylinder. Additionally we observe a negative solid body rotation, the so called "geostrophic mode", which results in a nearly standing fluid in the laboratory frame but is only of relevant magnitude for sufficiently high $Po$ values.
Furthermore, the axisymmetric double roll structure, which is considered to be the most important flow contribution in the context of potential dynamo action[26] can also be identified. This mode only appears is a narrow range roughly about $Po = 0.1$. In figure 14 we present an isosurface of the time averaged axial velocity field in the mantle frame of reference. The time averaging mostly cancels out the non-axisymmetric flow and only close to the end caps in the vicinity of the baffles some struc-

tures remain. In the bulk, however, the time averaged axial flow is dominated by the double roll structure. The observed flow structure and especially the occurrence of the double roll structure at a certain range of $Po$ values is consistent with previous studies on precession driven flows in a plain cylinder[26,107].

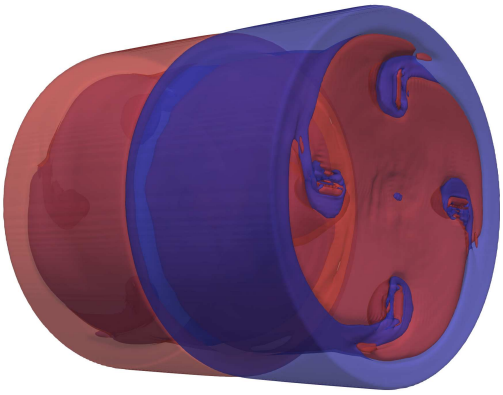

FIG. 14: Time averaged axial velocity $V_z$ in the mantle frame of the cylinder. Contours at $V_z = +1.5 \times 10^{-3}$ (red) and $V_z = -1.5 \times 10^{-3}$ (blue). This corresponds to about 7% of the maximum axial velocity. The baffles are extended to maximum blade depth $d_0$ and the Poincaré number is $Po = 0.1$. The time averaged flow is dominated by the double roll structure.

In the following we analyze the quantitative impact of the baffles in dependence on $Po$ and the immersion depth $d$ of the baffles for $d = 0, 0.5, 1, 1.5, 2\, d_0$.
In figure 15 the non-axialsymmetric part of the total energy is shown for different baffle depths. Although for baffle length $d = 0.5 d_0$ only a minor change is noticeable the deeper immersed baffles show a clear shift in the critical Poincaré number $Po_E^c$. This behavior is congruent with the suggestions made by Leorat[30]as the baffles at the end caps indeed shift the transition to higher Poincaré numbers. Also the maximum value and especially the non-axialsymmetric energy for $Po > Po_E^c$ are raised by the baffles of greater penetration depth. As a measure for $Po_E^c$ we chose the $Po$ just before the non-axialsymmetric energy drops as indicated by a black marker in the figure.

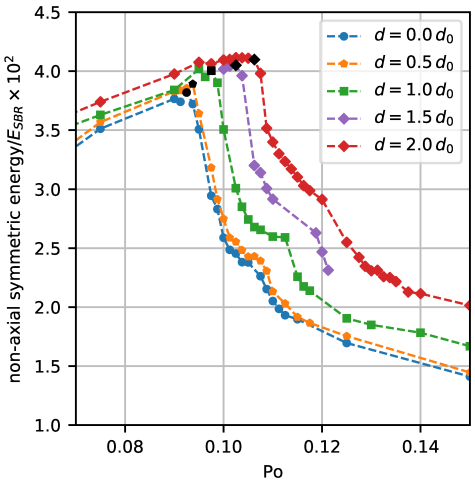


FIG. 15: The non-axialsymmetric energy as a function of $Po$ in the vicinity of the critical Poincaré number $Po_E^c$ for different baffle lengths $d$.

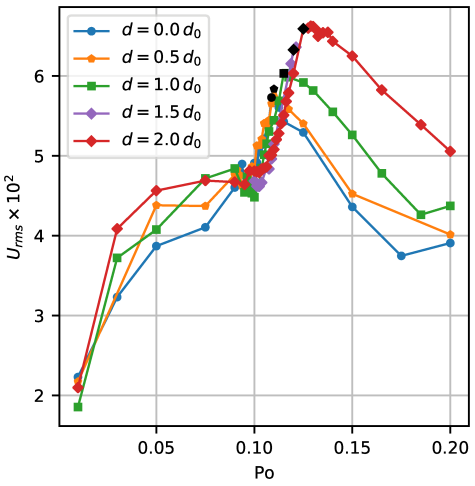


FIG. 16: The root-mean square velocity $U_{RMS}$ as a function of $Po$ in the vicinity of the critical Poincaré number $Po_U^c$ for different baffle lengths $d$..

Besides the maximum of the non-axialsymmetric energy a weakly pronounced bump is present in the region between $Po = 0.1$ and 0.12, which resembles

the 'plateau-like' behavior in previous studies without baffles.

As another characteristic quantity we consider the total root-mean-squared velocity $U_{rms} = \left[\int \left(\overline{U^2} - \overline{U}^2\right) \mathrm{d}V/V\right]^{1/2}$ which is connected to the turbulent kinetic energy as $T = 1/2\, U_{rms}^2$. The bar indicates the time average and $V$ is the total fluid volume. $U_{rms}$ as a function of $Po$ is shown in figure 16. Here also a maximum for all baffle depths is present which again is shifted to higher values of $Po$ for deeper baffles. This maximum in the turbulent energy correlates with the bump observed in the non-axialsymmetric energies. For $U_{rms}$ we define a second critical Poincaré number $Po_U^c$ as the first value after the sharp transition to the peak again marked black in the respective figure. Between $Po_E^c$ and $Po_U^c$ $U_{rms}$ shows a nearly linear behavior with comparable values for each baffle length. After the maximum the values of $U_{rms}$ differ strongly, with deeper baffles producing higher turbulence. Further at $Po_E^c$ the curves of $U_{rms}$ show an inflection point.

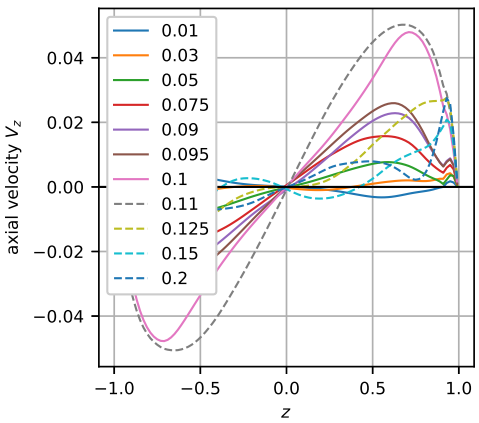


FIG. 17: Axial velocity along a line in axial direction at $r = 0.5$ for the cylinder with fully extended baffles ($d = d_0$).

To illustrate the development of the double roll structure we introduce a third critical Poincaré number $Po_z^c$, which is defined by the abrupt change of the structure of the axial velocity taken over a line in the axial direction with $(r, \phi) = (0.5, 0)$. The structure is depicted for the cylinder with baffles extended to the maximum immersion depth $d_0$ in figure 17. The profile looks nearly sinusoidal and grows with rising $Po$ and at some critical point declines again.

As a quantitative measure for the strength of the double roll we chose the maximum/minimum value of that velocity profile $V_{line}^{min/max}$. Its dependence on the Poincaré number is shown in figure 18 for the plain cylinder and baffles extended to $2d_0$.

For both setups shown in the figure as well as for baffle depths of $d = 1/2d_0$ and $d = 1\,d_0$ a clear maximum minimum of $v_{line}^{min/max}$ is observed. The critical Poincaré number regarding the double roll structure $Po_{DR}^c$ is taken as the mean value of the Poincaré numbers at which the minimum and the maximum value appear respectively. For the plain cylinder the Poincaré number of the extremum coincides with previous studies, whereas higher baffle lengths shift the extremum further to higher values of $Po$. Contrary to what the increase of the maximum energy of the directly forced flow with the addition of the baffles suggests (see fig. 15), the strength of the double roll structure remains nearly unaffected by the baffles. However, for $Po > Po_{DR}^c$ the amplitude of the double roll structure is drastically increased by the baffles. For small values of $Po$ the baffles do not have an significant impact on the double roll strength.

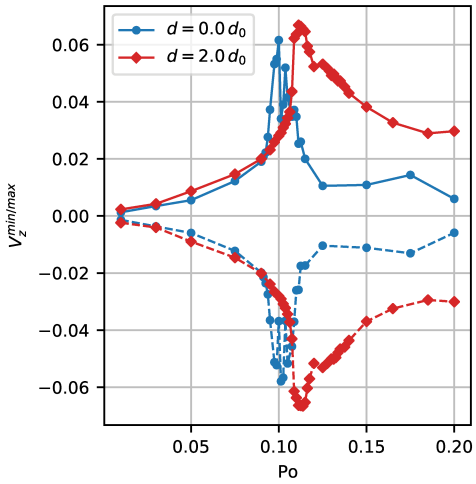


FIG. 18: The maximum (solid) / minimum (dashed) of the axial velocity over a line in axial direction at $r = 0.5$ for the plain cylinder and baffles extended to twice the maximum immersion depths $d_0$.

The results for the various critical Poinacaré numbers in dependence of the penetration depth of the baffles are summarized in figure 19 with an accuracy of $\Delta Po = 0.00125$.

Although the three different critical Poincaré numbers differ for each baffle length, they undergo a nearly similar trend as the baffle length is increased. The immersion of half extended blades just has a slight impact on all three

quantities but as the immersion depth increases all critical Poincaré numbers shift linearly with the baffle length. Fitting linear curves results in the following dependencies: $Po_E^c \propto 8.3 \times 10^{-3}\, d_0$, $Po_{DR}^c \propto 8.30 \times 10^{-3}\, d_0$ and $Po_U^c \propto 1 \times 10^{-2}\, d_0$, valid for blade lengths between $0.5\, d_0$ and $2\, d_0$.

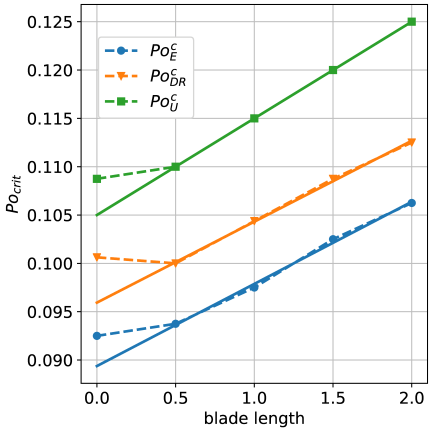


FIG. 19: Critical Poincaré numbers as defined above as functions of the Poincaré number (markers connected by dashed lines). The values for each critical Poincaré number are fitted by a linear curve for baffle lengths $\geq 0.5\, d_0$ (solid lines).

### 3. Symmetry Properties

Besides the shift of the critical Poincaré numbers a symmetrization of the flow is induced by the baffles. This is illustrated exemplarily by means of the time and azimuthal averaged velocity field in the turntable frame (see fig. 20).

As the time averaging procedure in the frame of the turntable averages out the forced mode, we obtain the double roll structure as the dominant mode. The baffles enforce the flow to a more symmetric form, thus suppressing higher modes with odd axial wave numbers. To quantify the symmetrization we consider the antisymmetric energy with respect to the cylinder center defined as $E_a = \frac{1}{2V}\int \mathbf{u}_a \mathrm{d}V$ with $\mathbf{u}_a = \frac{1}{2}\left(\overline{\mathbf{u}}(\mathbf{r}) + \overline{\mathbf{u}}(-\mathbf{r})\right)$. $\overline{\mathbf{u}}$ denotes the time averaged velocity field in the turntable frame.

As is evident from figure 21, $E_a$ decreases rapidly with increasing baffle length and for $d = d_0$ the flow is already near completely symmetric. Also a slight shift of the peak of $E_a$ to higher $Po$ values can be observed. That shift reflects well the trend discussed above for other characteristic flow quantities. However, the decline of the peak with increasing baffle length is too dominant as that this shift has any practical relevance.

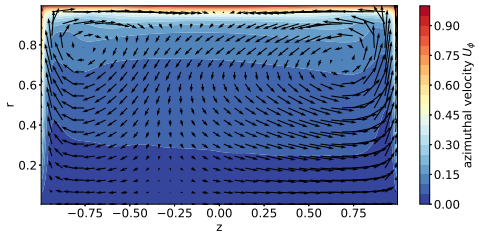


(a) $d = 0$

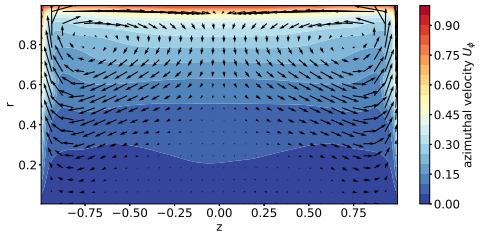


(b) $d = d_0$

FIG. 20: Azimuthal averaged velocity field in the turntable frame. The azimuthal velocity is color coded whereas the meridional velocity is visualized by the arrows. The field is shown for two different baffle length: (a) $d = 0$, (b) $d = d_0$. Note the increased symmetry for the case of immersed baffles.

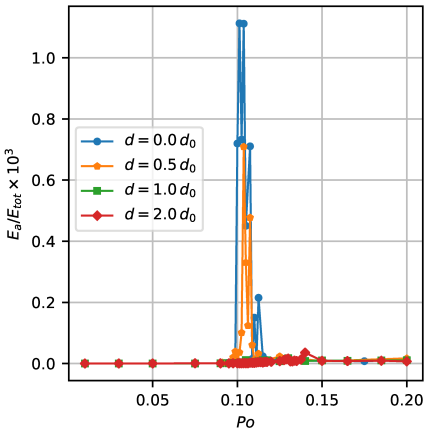


FIG. 21: Antisymmetric energy $E_a$ scaled by the total kinetic energy $E_{tot}$ for different penetration depths of the baffles.

## VI. CONCLUSION

In this paper we present the newly developed pseudo-spectral code SpecDyn based on a direct forcing Immersed Boundary Method that allows simulations of hydrodynamic flows in arbitrary vessel geometries. We deployed the code to study the flow in a cylinder impacted by a particular set-up of four baffles mounted symmetrically on the inner side of each end cap. This design corresponds to the geometry of the planned precession dynamo experiment at HZDR where a fluid flow of liquid sodium contained in a precessing cylinder will be used to excite and sustain a magnetohydrodynamic dynamo. In that experiment such a configuration of baffles may be used in order to have another possibility to adjust the fluid flow. Although, the construction of the experiment is already too far advanced for the results to force any changes to the design, the results are beneficial for the planning of experimental campaigns and the very control of the experiment. Furthermore, the simulations with baffles confirm previous, more hand-waving assumptions about the transition of flow regimes in the planned precession dynamo experiment.

To prove the reliability and robustness of the code, we started with a simple model of the spin-up in the cylinder. The behavior of the spin-up time is in agreement with the scaling as expected from theoretical considerations (see e.g.[103]) and shows a plausible acceleration of the spin-up when inserting baffles into the fluid flow. We found the spin-up time to decrease with increasing baffle length, especially for larger $Re$, with the Reynolds number ranging up to $Re = 6400$ in the numerical experiments. Similar behavior was found in experiments of *Burmann & Noir*[108] who used bumps at the bottom of a spinning cylinder to increase the viscous coupling at the boundary. However, since the configuration examined in this study is a unique for the precession dynamo experiment planned at HZDR a direct comparison of outcome is not possible.

When considering the impact of baffles on the precession driven flow we find a remarkable small impact on the the main characteristic features of the flow, i.e. the amplitude of the forced mode as well as the emergence of the double roll structure, which anticipates the transition to the turbulent regime, behave in a similar way. To quantify the impact of the baffles we considered three characteristic values of the Poincaré number $Po$ that mark the transition of the flow. Specifically, these are the abrupt drop of the non-axisymmetric energy, the maximum of the amplitude of the double roll structure, and the maximum of the root-mean-square velocity $U_{\mathrm{rms}}$ as a measure for the turbulent kinetic energy. We observe an increase of the strength of the considered quantities, which can be explained by the increase of the flow forcing due to the baffles. Furthermore, and as expected, by increasing the penetration depth of the baffles, the flow transitions are shifted to larger Poincaré numbers.

In the present study we focus on the large scale structure of the flow and mostly on time-averaged quantities, because it is supposed that these features are most important for the dynamo. However, we also included statistical features of turbulence, like the root mean square velocity, which shows that the presence of baffles indeed increases the level of fluctuations. Nevertheless, within the parameters examined in our study the large scale features of the flow are only slightly altered so that we may conclude that the presence of blades does not trigger any novel instability or transition of the flow. An important result, and so not necessarily predictable, is the fact that above the critical Poincaré numbers characteristic quantities, like flow amplitudes or turbulence intensity ($U^2_{\mathrm{rms}}$), remain on a higher level when comparing with the case without baffles. Thus, with the help of the baffles it is possible to inject a larger amount of kinetic energy into the flow, even if the overall effect remains small, which is not surprising given the rather small penetration depth of the baffles.

Regarding the influence of the baffles on the ability of the flow to drive a dynamo, the results remain ambiguous. On the one hand, baffles give a higher flow energy in the large scale flow modes, which should be beneficial for a dynamo. On the other hand, an increased contribution of disordered small-scale turbulence usually hampers the dynamo process due to the increased effective magnetic diffusivity. Based on the results of simulations of precession-driven dynamos in spherical geometry *Tilgner*[13] suggested, that symmetry breaking of the flow is necessary to obtain a dynamo at all . Our simulations, however, reveal a clear symmetrization of the flow field due to the presence of the baffles, which is equiv-

alent to the suppression of flow components with odd axial wavenumber. Thus when transferring the results of *Tilgner*[13] to our case, it may be that the presence of baffles is counter-effective for the dynamo. How robust this effect is, and whether the opposite, i.e. an advantage due to symmetrization because of a more distinct shape and a larger amplitude of the double-roll structure, will only become clear in future models that take into account magnetic fields by means of the induction equation in the next expansion stage of the *SpecDyn* code.

## ACKNOWLEDGMENTS

This work benefited from support through projects GR 967/7-1 and GI 1405/1-1 of the Deutsche Forschungsgesellschaft. The authors gratefully acknowledge the Gauss Centre for Supercomputing e.V. (www.gauss-centre.eu) for funding this project by providing computing time through the John von Neumann Institute for Computing (NIC) on the GCS Supercomputer JUWELS[98] at Jülich Supercomputing Centre (JSC). The authors also thank Federico Pizzi from HZDR for providing data from his simulations of precession-driven flows with the code SEMTEX.

## REFERENCES

[1]P. Meunier, "Geoinspired soft mixers," J. Fluids Mech. **903**, A15 (2020).
[2]H. Poincaré, "Sur la précession des corps déformables," Bulletin Astronomique I, **27**, 321–356 (1910).
[3]R. R. Kerswell, "The instability of precessing flow," Geophys. Astrophys. Fluid Dyn. **72**, 107–144 (1993).
[4]R. R. Kerswell, "Secondary instabilities in rapidly rotating fluids: inertial wave breakdown," J. Fluids Mech. **382**, 283–306 (1999).
[5]S. Goto, A. Matsunaga, M. Fujiwara, M. Nishioka, S. Kida, M. Yamato, and S. Tsuda, "Turbulence driven by precession in spherical and slightly elongated spheroidal cavities," Phys. Fluids **26**, 055107 (2014), 10.1063/1.4874695.
[6]Y. Lin, P. Marti, and J. Noir, "Shear-driven parametric instability in a precessing sphere," Phys. Fluids **27**, 046601 (2015), 10.1063/1.4916234.
[7]J. Noir, P. Cardin, D. Jault, and J.-P. Masson, "Experimental evidence of non-linear resonance effects between retrograde precession and the tilt-over mode within a spheroid," Geophys. J. Int. **154**, 407–416 (2003).
[8]R. Hollerbach and R. R. Kerswell, "Oscillatory internal shear layers in rotating and precessing flows," J. Fluids Mech. **298**, 327–339 (1995).
[9]S. Lorenzani and A. Tilgner, "Fluid instabilities in precessing spheroidal cavities," J. Fluids Mech. **447**, 111–128 (2001).
[10]F. H. Busse, "Steady fluid flow in a precessing spheroidal shell," J. Fluids Mech. **33**, 739–751 (1968).
[11]W. V. R. Malkus, "Precession of the Earth as the Cause of Geomagnetism," Science **160**, 259–264 (1968).
[12]J. P. Vanyo, "A geodynamo powered by luni-solar precession," Geophys. Astrophys. Fluid Dyn. **59**, 209–234 (1991).
[13]A. Tilgner, "Precession driven dynamos," Phys. Fluids **17**, 034104 (2005).
[14]C. A. Dwyer, D. J. Stevenson, and F. Nimmo, "A long-lived lunar dynamo driven by continuous mechanical stirring," Nature (London) **479**, 212–214 (2011).
[15]J. Noir and D. Cébron, "Precession-driven flows in non-axisymmetric ellipsoids," J. Fluids Mech. **737**, 412–439 (2013).
[16]B. P. Weiss and S. M. Tikoo, "The lunar dynamo," Science **346**, 1198 (2014).
[17]C.-C. Wu and P. Roberts, "On a dynamo driven by topographic precession," Geophys. Astrophys. Fluid Dyn. **103**, 467–501 (2009).
[18]C. Nore, J. Léorat, J.-L. Guermond, and F. Luddens, "Nonlinear dynamo action in a precessing cylindrical container," Phys. Rev. E **84**, 016317 (2011).
[19]O. Goepfert and A. Tilgner, "Dynamos in precessing cubes," New J. Phys. **18**, 103019 (2016), 10.1088/1367-2630/18/10/103019.
[20]Y. Lin, P. Marti, J. Noir, and A. Jackson, "Precession-driven dynamos in a full sphere and the role of large scale cyclonic vortices," Phys. Fluids **28**, 066601 (2016), 10.1063/1.4954295.
[21]D. Cébron, R. Laguerre, J. Noir, and N. Schaeffer, "Precessing spherical shells: flows, dissipation, dynamo and the lunar core," Geophys. J. Int. **219**, S34–S57 (2019).
[22]F. Stefani, S. Eckert, G. Gerbeth, A. Giesecke, T. Gundrum, C. Steglich, T. Weier, and B. Wustmann, "DRESDYN – a new facility for MHD experiments with liquid sodium," Magnetohydrodynamics **48**, 103–114 (2012).
[23]F. Stefani, T. Albrecht, G. Gerbeth, A. Giesecke, T. Gundrum, J. Herault, C. Nore, and C. Steglich, "Towards a precession driven dynamo experiment," Magnetohydrodynamics **51**, 275–284 (2015).
[24]R. F. Gans, "On the precession of a resonant cylinder," J. Fluids Mech. **41**, 865–872 (1970).
[25]R. F. Gans, "On hydromagnetic precession in a cylinder," J. Fluids Mech. **45**, 111–130 (1971).
[26]A. Giesecke, T. Vogt, T. Gundrum, and F. Stefani, "Nonlinear large scale flow in a precessing cylinder and its ability to drive dynamo action," Phys. Rev. Lett. **120**, 024502 (2018), 10.1103/PhysRevLett.120.024502.
[27]A. Giesecke, T. Vogt, T. Gundrum, and F. Stefani, "Kinematic dynamo action of a precession-driven flow based on the results of water experiments and hydrodynamic simulations." Geophys. Astrophys. Fluid Dyn. **113**, 235–255 (2019).
[28]J. Herault, T. Gundrum, A. Giesecke, and F. Stefani, "Subcritical transition to turbulence of a precessing flow in a cylindrical vessel," Phys. Fluids **27**, 124102 (2015), 10.1063/1.4936653.
[29]J. Léorat, P. Lallemand, J. Guermond, and F. Plunian, "Dynamo action, between numerical experiments and liquid sodium devices," in *Dynamo and Dynamics, a mathematical challenge*, Vol. 26, edited by P. Chossat, D. Ambruster, and I. Oprea (Springer, Dordrecht, Netherlands, 2001) pp. 25–33.
[30]J. Léorat, "Large scales features of a flow driven by precession," Magnetohydrodynamics **42**, 143–151 (2006).
[31]J. M. Lopez and F. Marques, "Nonlinear and detuning effects of the nutation angle in precessionally forced rotating cylinder flow," Phys. Rev. Fluids **1**, 023602 (2016), 10.1103/PhysRevFluids.1.023602.
[32]T. Albrecht, H. M. Blackburn, J. M. Lopez, R. Manasseh, and P. Meunier, "On triadic resonance as an instability mechanism in precessing cylinder flow," J. Fluids Mech. **841**, R3 (2018).
[33]J. P. Vanyo and P. W. Likins, "Use of Baffles to Suppress Energy Dissipation in Liquid-Filled Precessing Cavities," J. Spacecraft Rockets **10**, 627 (1973).
[34]D. S. Zimmerman, S. A. Triana, H.-C. Nataf, and D. P. Lathrop, "A turbulent, high magnetic Reynolds number experimental model of Earth's core," J. Geophys. Res. (Solid Earth) **119**, 4538–4557 (2014).
[35]K. Finke and A. Tilgner, "Simulations of the kinematic dynamo onset of spherical Couette flows with smooth and rough boundaries," Phys. Rev. E **86**, 016310 (2012), 10.1103/PhysRevE.86.016310.

[36]R. Monchaux, M. Berhanu, M. Bourgoin, M. Moulin, P. Odier, J.-F. Pinton, R. Volk, S. Fauve, N. Mordant, F. Pétrélis, A. Chiffaudel, F. Daviaud, B. Dubrulle, C. Gasquet, L. Marié, and F. Ravelet, "Generation of a Magnetic Field by Dynamo Action in a Turbulent Flow of Liquid Sodium," Phys. Rev. Lett. **98**, 044502 (2007), 10.1103/PhysRevLett.98.044502.

[37]S. Miralles, N. Bonnefoy, M. Bourgoin, P. Odier, J.-F. Pinton, N. Plihon, G. Verhille, J. Boisson, F. Daviaud, and B. Dubrulle, "Dynamo threshold detection in the von kármán sodium experiment," Phys. Rev. E **88**, 013002 (2013).

[38]A. Giesecke, C. Nore, F. Stefani, G. Gerbeth, J. Léorat, W. Herreman, F. Luddens, and J.-L. Guermond, "Influence of high-permeability discs in an axisymmetric model of the Cadarache dynamo experiment," New J. Phys. **14**, 053005 (2012), 10.1088/1367-2630/14/5/053005.

[39]C. Nore, J. Léorat, J.-L. Guermond, and A. Giesecke, "Mean-field model of the von Kármán sodium dynamo experiment using soft iron impellers," Phys. Rev. E **91**, 013008 (2015).

[40]S. Kreuzahler, D. Schulz, H. Homann, Y. Ponty, and R. Grauer, "Numerical study of impeller-driven von Kármán flows via a volume penalization method," New J. Phys. **16**, 103001 (2014), 10.1088/1367-2630/16/10/103001.

[41]S. Kreuzahler, Y. Ponty, N. Plihon, H. Homann, and R. Grauer, "Dynamo enhancement and mode selection triggered by high magnetic permeability," Phys. Rev. Lett. **119**, 234501 (2017).

[42]C. Nore, D. Castanon Quiroz, L. Cappanera, and J.-L. Guermond, "Direct numerical simulation of the axial dipolar dynamo in the Von Kármán Sodium experiment," Europhys. Lett. **114**, 65002 (2016).

[43]F. Pizzi, A. Giesecke, and F. Stefani, "Ekman boundary layers in a fluid filled precessing cylinder," AIP Advances **11**, 035023 (2021).

[44]F. Pizzi, A. Giesecke, J. Šimkanin, and F. Stefani, "Prograde and retrograde precession of a fluid -filled cylinder," New J. Phys. **23**, 123016 (2021).

[45]J. W. Cooley and J. W. Tukey, "An algorithm for the machine calculation of complex fourier series," Mathematics of computation **19**, 297–301 (1965).

[46]C. Canuto, M. Y. Hussaini, A. Quarteroni, and T. A. Zang, *Spectral methods: fundamentals in single domains* (Springer Science & Business Media, 2007).

[47]J. P. Boyd, *Chebyshev and Fourier spectral methods* (Courier Corporation, 2001).

[48]G. Patterson Jr and S. A. Orszag, "Spectral calculations of isotropic turbulence: Efficient removal of aliasing interactions," The Physics of Fluids **14**, 2538–2541 (1971).

[49]C.-W. Shu and S. Osher, "Efficient implementation of essentially non-oscillatory shock-capturing schemes," Journal of computational physics **77**, 439–471 (1988).

[50]S. Gottlieb, C.-W. Shu, and E. Tadmor, "Strong stability-preserving high-order time discretization methods," SIAM review **43**, 89–112 (2001).

[51]A. J. Chorin, "Numerical solution of the navier-stokes equations," Mathematics of computation **22**, 745–762 (1968).

[52]R. Temam, "Sur l'approximation de la solution des équations de navier-stokes par la méthode des pas fractionnaires (ii)," Archive for rational mechanics and analysis **33**, 377–385 (1969).

[53]R. Temam, *Navier-Stokes equations: theory and numerical analysis*, Vol. 343 (American Mathematical Soc., 2001).

[54]C. S. Peskin, "Numerical analysis of blood flow in the heart," Journal of computational physics **25**, 220–252 (1977).

[55]W.-X. Huang and F.-B. Tian, "Recent trends and progress in the immersed boundary method," Proceedings of the Institution of Mechanical Engineers, Part C: Journal of Mechanical Engineering Science **233**, 7617–7636 (2019).

[56]D. Goldstein, R. Handler, and L. Sirovich, "Modeling a no-slip flow boundary with an external force field," Journal of computational physics **105**, 354–366 (1993).

[57]D. Goldstein, R. Handler, and L. Sirovich, "Direct numerical simulation of turbulent flow over a modeled riblet covered surface," Journal of Fluid Mechanics **302**, 333–376 (1995).

[58]E. Saiki and S. Biringen, "Numerical simulation of a cylinder in uniform flow: application of a virtual boundary method," Journal of computational physics **123**, 450–465 (1996).

[59]M.-C. Lai and C. S. Peskin, "An immersed boundary method with formal second-order accuracy and reduced numerical viscosity," Journal of computational Physics **160**, 705–719 (2000).

[60]G. Iaccarino and R. Verzicco, "Immersed boundary technique for turbulent flow simulations," Appl. Mech. Rev. **56**, 331–347 (2003).

[61]R. Mittal and G. Iaccarino, "Immersed boundary methods," Annu. Rev. Fluid Mech. **37**, 239–261 (2005).

[62]E. Arquis, J. Caltagirone, *et al.*, "Sur les conditions hydrodynamiques au voisinage d'une interface milieu fluide-milieu poreux: applicationa la convection naturelle," CR Acad. Sci. Paris II **299**, 1–4 (1984).

[63]G. H. Keetels, H. Clercx, and G. van Heijst, "Fourier spectral solver for the incompressible navier-stokes equations with volume-penalization," in *International Conference on Computational Science* (Springer, 2007) pp. 898–905.

[64]C. Jause-Labert, F. S. Godeferd, and B. Favier, "Numerical validation of the volume penalization method in three-dimensional pseudo-spectral simulations," Computers & fluids **67**, 41–56 (2012).

[65]E. Fadlun, R. Verzicco, P. Orlandi, and J. Mohd-Yusof, "Combined immersed-boundary finite-difference methods for three-dimensional complex flow simulations," Journal of computational physics **161**, 35–60 (2000).

[66]A. Cristallo and R. Verzicco, "Combined immersed boundary/large-eddy-simulations of incompressible three dimensional complex flows," Flow, turbulence and combustion **77**, 3–26 (2006).

[67]T. Engels, D. Kolomenskiy, K. Schneider, F.-O. Lehmann, and J. Sesterhenn, "Bumblebee flight in heavy turbulence," Physical review letters **116**, 028103 (2016).

[68]J. A. Morales, W. J. Bos, K. Schneider, and D. C. Montgomery, "Magnetohydrodynamically generated toroidal and poloidal velocities in confined plasma," in *APS Division of Plasma Physics Meeting Abstracts*, Vol. 2013 (2013) pp. TO5–003.

[69]J. A. Morales, M. Leroy, W. J. Bos, and K. Schneider, "Simulation of confined magnetohydrodynamic flows with dirichlet boundary conditions using a pseudo-spectral method with volume penalization," Journal of Computational Physics **274**, 64–94 (2014).

[70]K. Schneider, "Immersed boundary methods for numerical simulation of confined fluid and plasma turbulence in complex geometries: a review," Journal of Plasma Physics **81** (2015).

[71]J. Mohd-Yusof, "Combined immersed boundary/b-spline method for simulations of flows in complex geometries in complex geometries ctr annual research briefs, nasa ames," NASA Ames/Stanford University (1997).

[72]R. Verzicco, J. Mohd-Yusof, P. Orlandi, and D. Haworth, "Les in complex geometries using boundary body forces," in *Proceedings of the summer program* (Center for Turbulence Research Stanford, CA, USA, 1998) pp. 171–186.

[73]S. Kreuzahler, D. Schulz, H. Homann, Y. Ponty, and R. Grauer, "Numerical study of impeller-driven von kármán flows via a volume penalization method," New Journal of Physics **16**, 103001 (2014).

[74]E. Balaras, "Modeling complex boundaries using an external force field on fixed cartesian grids in large-eddy simulations," Computers & Fluids **33**, 375–404 (2004).

[75]A. Gilmanov, F. Sotiropoulos, and E. Balaras, "A general reconstruction algorithm for simulating flows with complex 3d immersed boundaries on cartesian grids," Journal of Computational Physics **191**, 660–669 (2003).

[76]A. Gilmanov and F. Sotiropoulos, "A hybrid cartesian/immersed boundary method for simulating flows with 3d, geometrically complex, moving bodies," Journal of computational physics **207**, 457–492 (2005).

[77]L. Ge and F. Sotiropoulos, "A numerical method for solving the 3d unsteady incompressible navier–stokes equations in curvilinear domains with complex immersed boundaries," Journal of computational physics **225**, 1782–1809 (2007).
[78]I. Borazjani, L. Ge, and F. Sotiropoulos, "Curvilinear immersed boundary method for simulating fluid structure interaction with complex 3d rigid bodies," Journal of Computational physics **227**, 7587–7620 (2008).
[79]Y. v. H. Juergen Riegel, Werner Mayer, "Freecad," (2022).
[80]Geuzaine, Christophe and Remacle, Jean-Francois, "Gmsh," (2022).
[81]A. Narkhede and D. Manocha, "Fast polygon triangulation based on seidel's algorithm," in *Graphics Gems V* (Elsevier, 1995) pp. 394–397.
[82]S. Woop, C. Benthin, and I. Wald, "Watertight ray/triangle intersection," Journal of Computer Graphics Techniques (JCGT) **2**, 65–82 (2013).
[83]T. Ikeno and T. Kajishima, "Finite-difference immersed boundary method consistent with wall conditions for incompressible turbulent flow simulations," Journal of Computational Physics **226**, 1485–1508 (2007).
[84]T.-L. Horng, P.-W. Hsieh, S.-Y. Yang, and C.-S. You, "A simple direct-forcing immersed boundary projection method with prediction-correction for fluid-solid interaction problems," Computers & Fluids **176**, 135–152 (2018).
[85]R. Rannacher, "On chorin's projection method for the incompressible navier-stokes equations, in" navier-stokes equations: Theory and numerical methods"(r. rautmann, et al., eds.)," in *Proc. Oberwolfach Conf*, Vol. 19 (1991).
[86]J.-L. Guermond, P. Minev, and J. Shen, "An overview of projection methods for incompressible flows," Computer methods in applied mechanics and engineering **195**, 6011–6045 (2006).
[87]J. Van Kan, "A second-order accurate pressure-correction scheme for viscous incompressible flow," SIAM journal on scientific and statistical computing **7**, 870–891 (1986).
[88]K. Goda, "A multistep technique with implicit difference schemes for calculating two-or three-dimensional cavity flows," Journal of computational physics **30**, 76–95 (1979).
[89]L. J. Timmermans, P. D. Minev, and F. N. Van De Vosse, "An approximate projection scheme for incompressible flow using spectral elements," International journal for numerical methods in fluids **22**, 673–688 (1996).
[90]J. Guermond and J. Shen, "On the error estimates for the rotational pressure-correction projection methods," Mathematics of Computation **73**, 1719–1737 (2004).
[91]D. Pekurovsky, "P3dfft: A framework for parallel computations of fourier transforms in three dimensions," SIAM Journal on Scientific Computing **34**, C192–C209 (2012).
[92]N. Li and S. Laizet, "2decomp & fft-a highly scalable 2d decomposition library and fft interface," in *Cray user group 2010 conference* (2010) pp. 1–13.
[93]M. Pippig, "Pfft: An extension of fftw to massively parallel architectures," SIAM Journal on Scientific Computing **35**, C213–C236 (2013).
[94]K. G. Larkin, M. A. Oldfield, and H. Klemm, "Fast fourier method for the accurate rotation of sampled images," Optics communications **139**, 99–106 (1997).
[95]L. Dalcin, M. Mortensen, and D. E. Keyes, "Fast parallel multidimensional fft using advanced mpi," Journal of Parallel and Distributed Computing **128**, 137–150 (2019).
[96]Message Passing Interface Forum, *MPI: A Message-Passing Interface Standard Version 4.0* (2021).
[97]M. Frigo and S. G. Johnson, "The design and implementation of FFTW3," Proceedings of the IEEE **93**, 216–231 (2005), special issue on "Program Generation, Optimization, and Platform Adaptation".
[98]D. Krause, "Juwels: Modular tier-0/1 supercomputer at the jülich supercomputing centre," Journal of large-scale research facilities JLSRF **5**, A135–A135 (2019).
[99]E. Benton and A. Clark Jr, "Spin-up," Annual Review of Fluid Mechanics **6**, 257–280 (1974).
[100]P. Duck and M. Foster, "Spin-up of homogeneous and stratified fluids," Annual review of fluid mechanics **33**, 231–263 (2001).
[101]J. S. Park and J. M. Hyun, "Review on open-problems of spin-up flow of an incompressible fluid," Journal of mechanical science and technology **22**, 780–787 (2008).
[102]H. Greenspan and L. Howard, "On a time-dependent motion of a rotating fluid," Journal of fluid mechanics **17**, 385–404 (1963).
[103]H. P. Greenspan, "The theory of rotating fluids," Tech. Rep. (Massachusetts Inst of Tech Cambridge Dept of Mathematics, 1968).
[104]E. Wedemeyer, "The unsteady flow within a spinning cylinder," Journal of Fluid Mechanics **20**, 383–399 (1964).
[105]G. Venezian, "Spin-up of a contained fluid." Tech. Rep. (CALIFORNIA INST OF TECH PASADENA DIV OF ENGINEERING AND APPLIED SCIENCE, 1969).
[106]A. Giesecke, T. Albrecht, T. Gundrum, J. Herault, and F. Stefani, "Triadic resonances in nonlinear simulations of a fluid flow in a precessing cylinder," New J. Phys. **17**, 113044 (2015), 10.1088/1367-2630/17/11/113044.
[107]F. Pizzi, A. Giesecke, J. Šimkanin, and F. Stefani, "Prograde and retrograde precession of a fluid-filled cylinder," New Journal of Physics **23**, 123016 (2021).
[108]F. Burmann and J. Noir, "Effects of bottom topography on the spin-up in a cylinder," Phys. Fluids **30** (2018), 10.1063/1.5051111.

PLEASE CITE THIS ARTICLE AS DOI: 10.1063/5.0110153

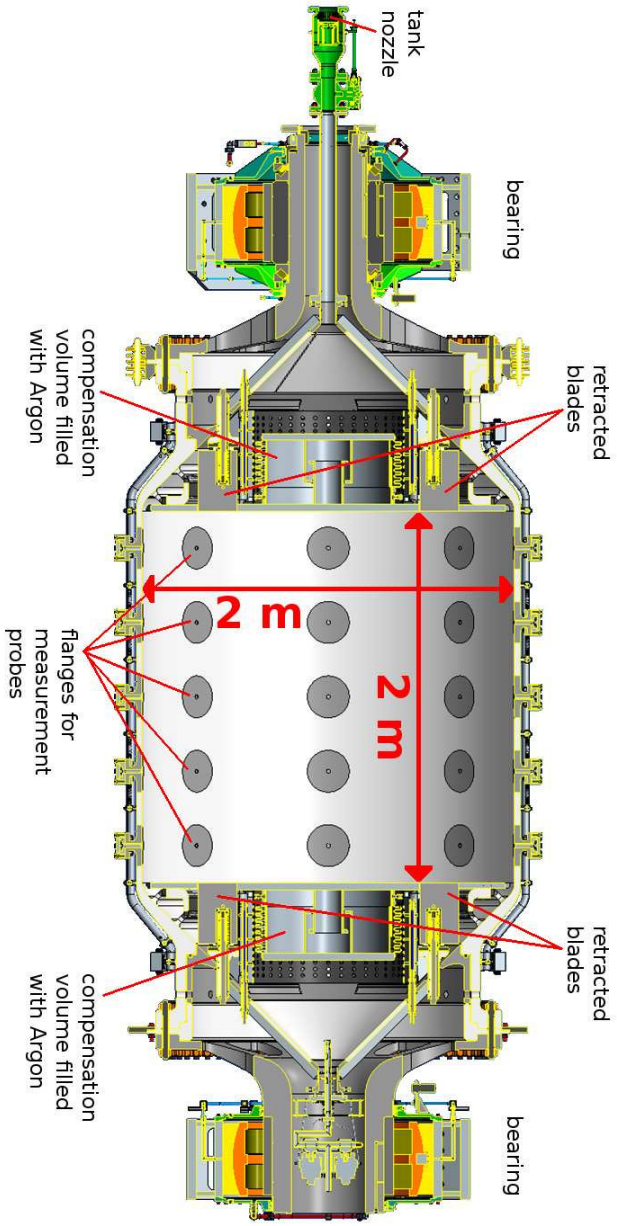

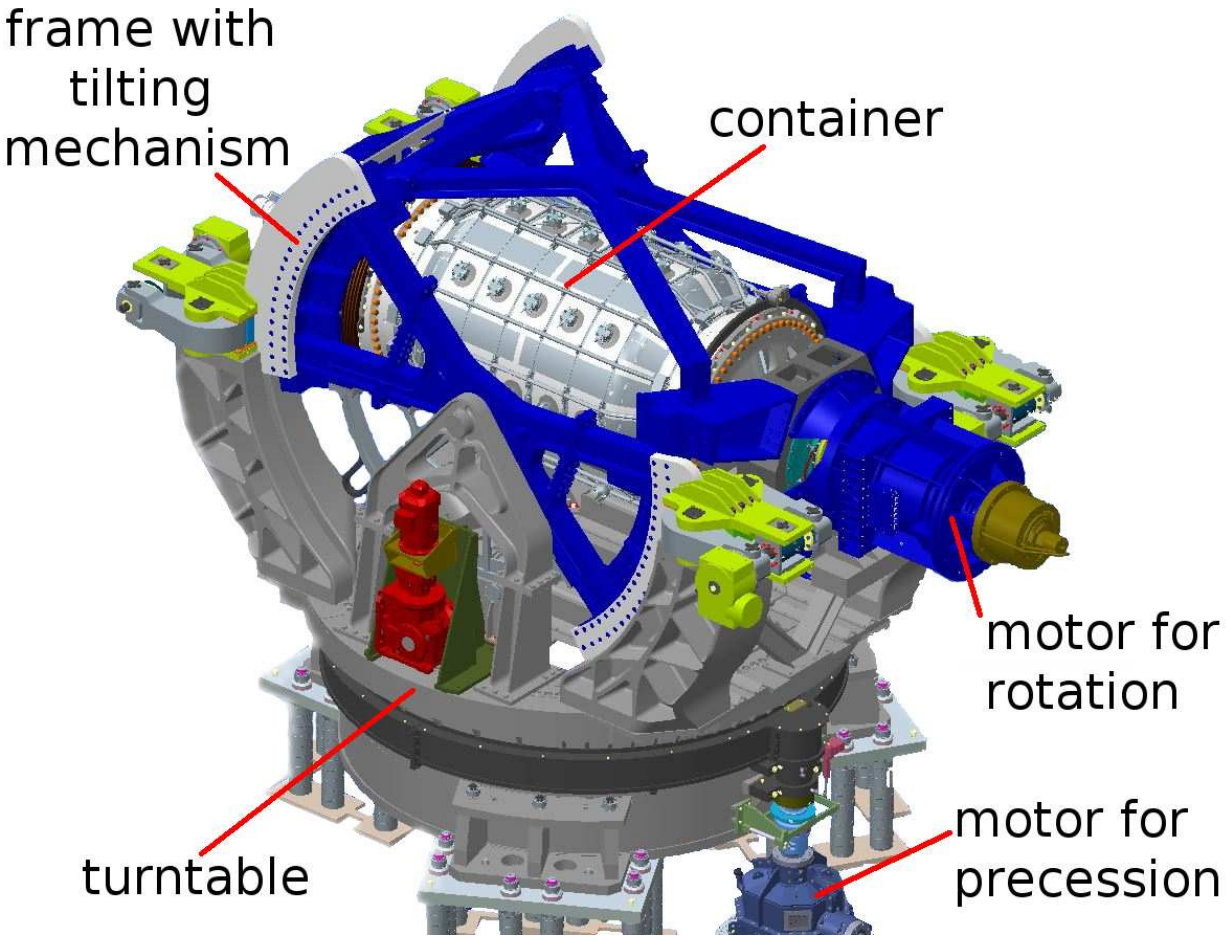

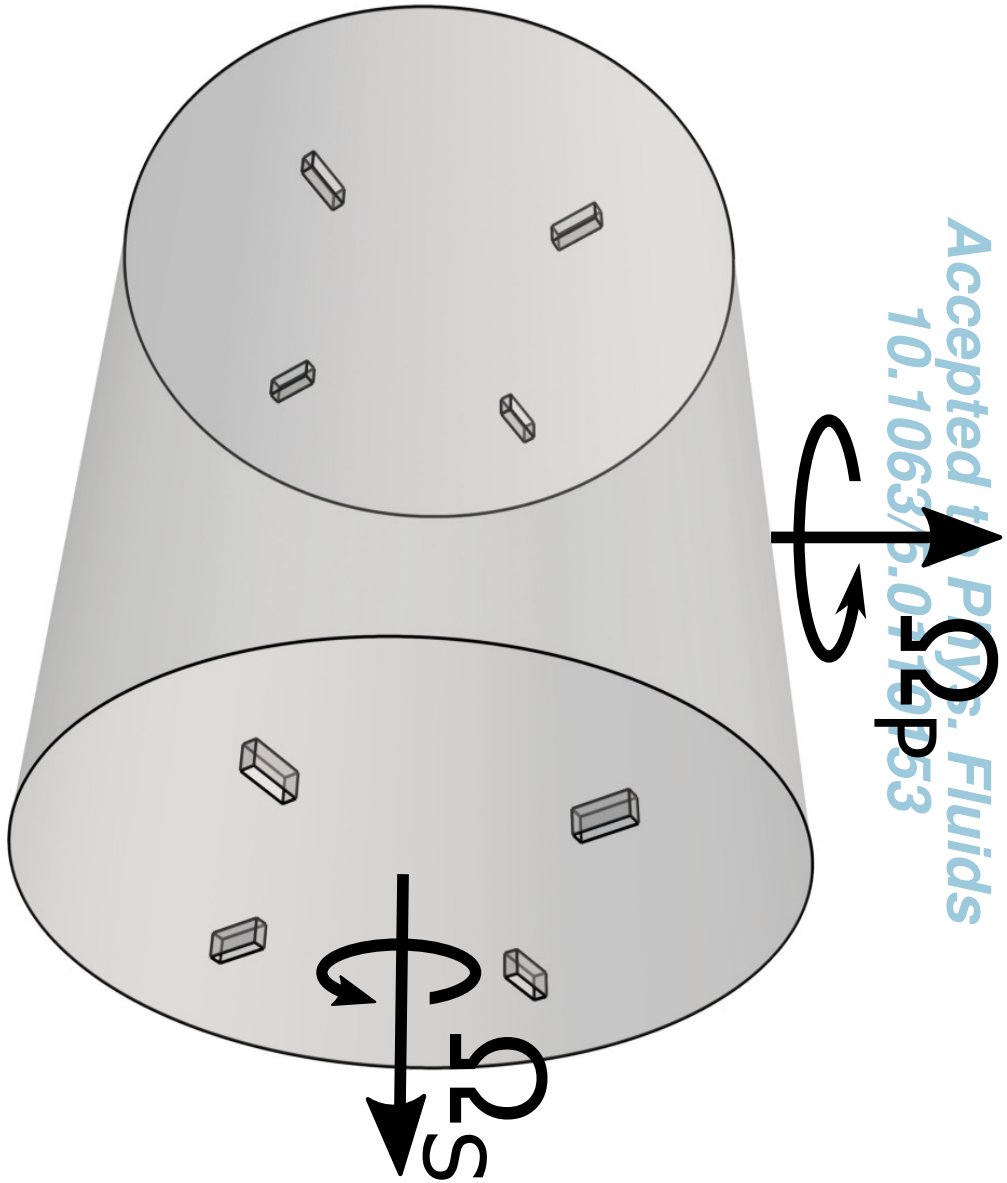

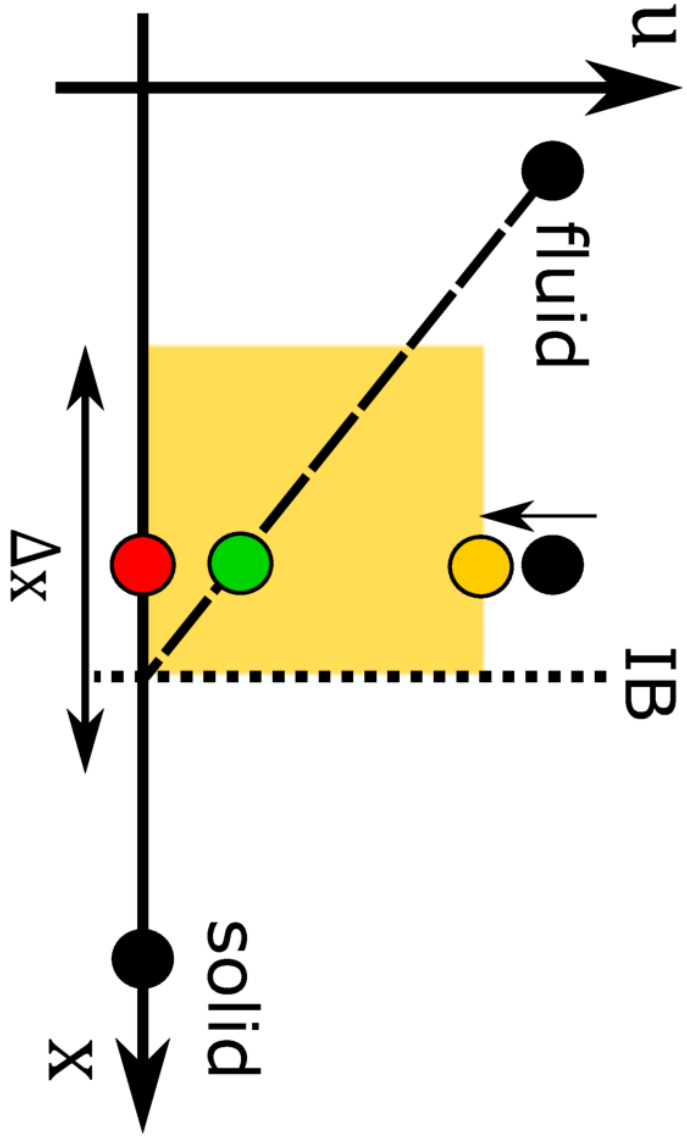

PLEASE CITE THIS ARTICLE AS DOI: 10.1063/5.0110153

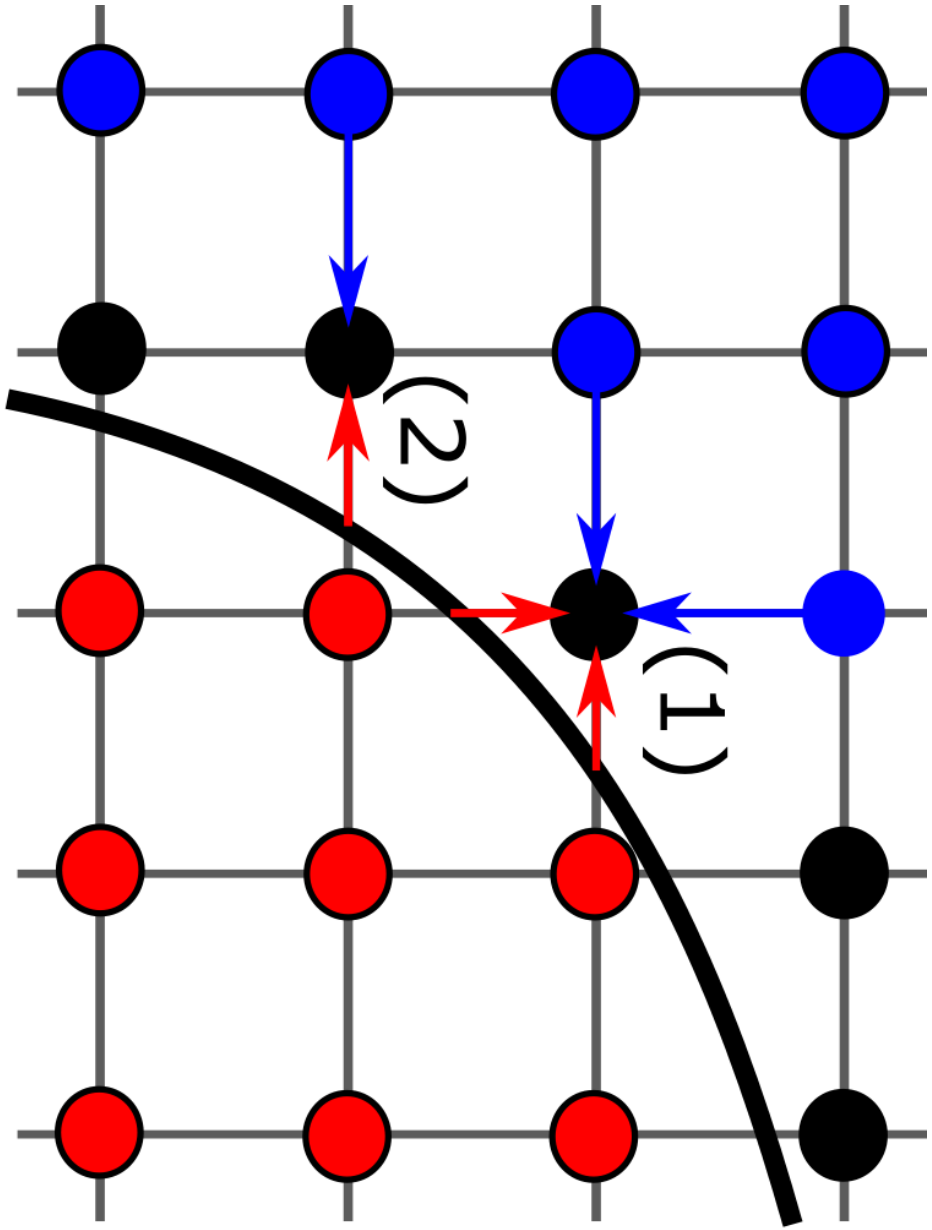

PLEASE CITE THIS ARTICLE AS DOI: 10.1063/5.0110153

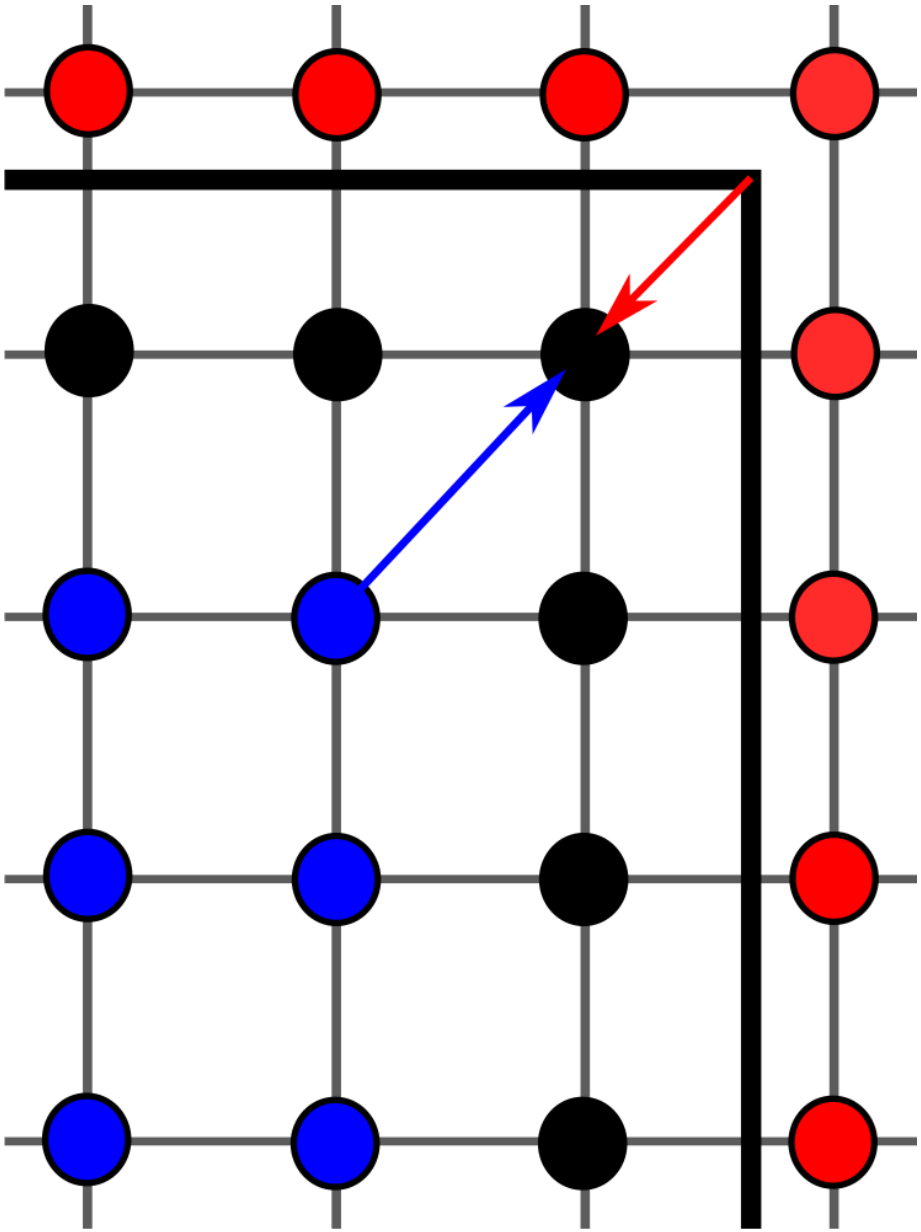

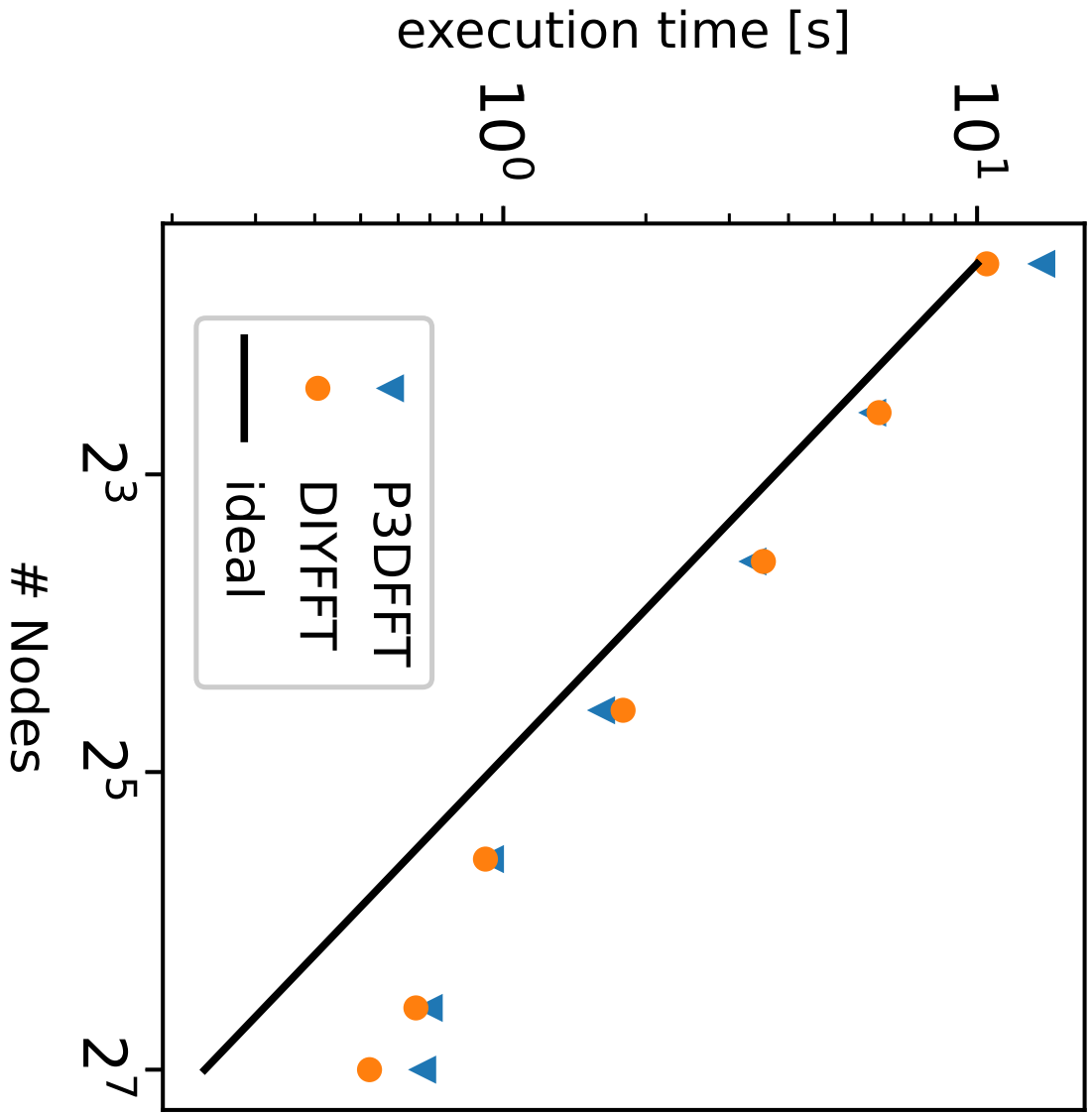

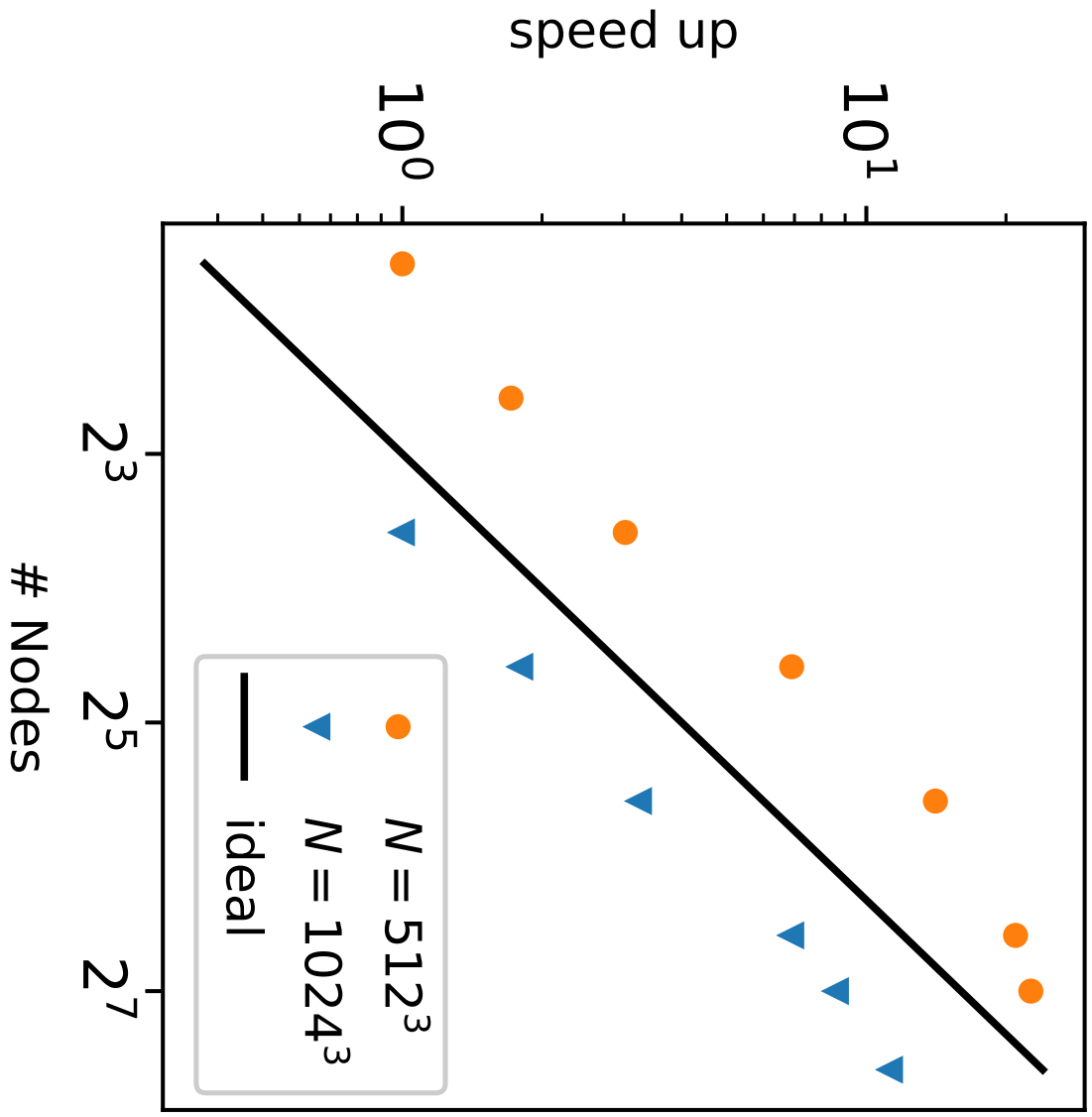

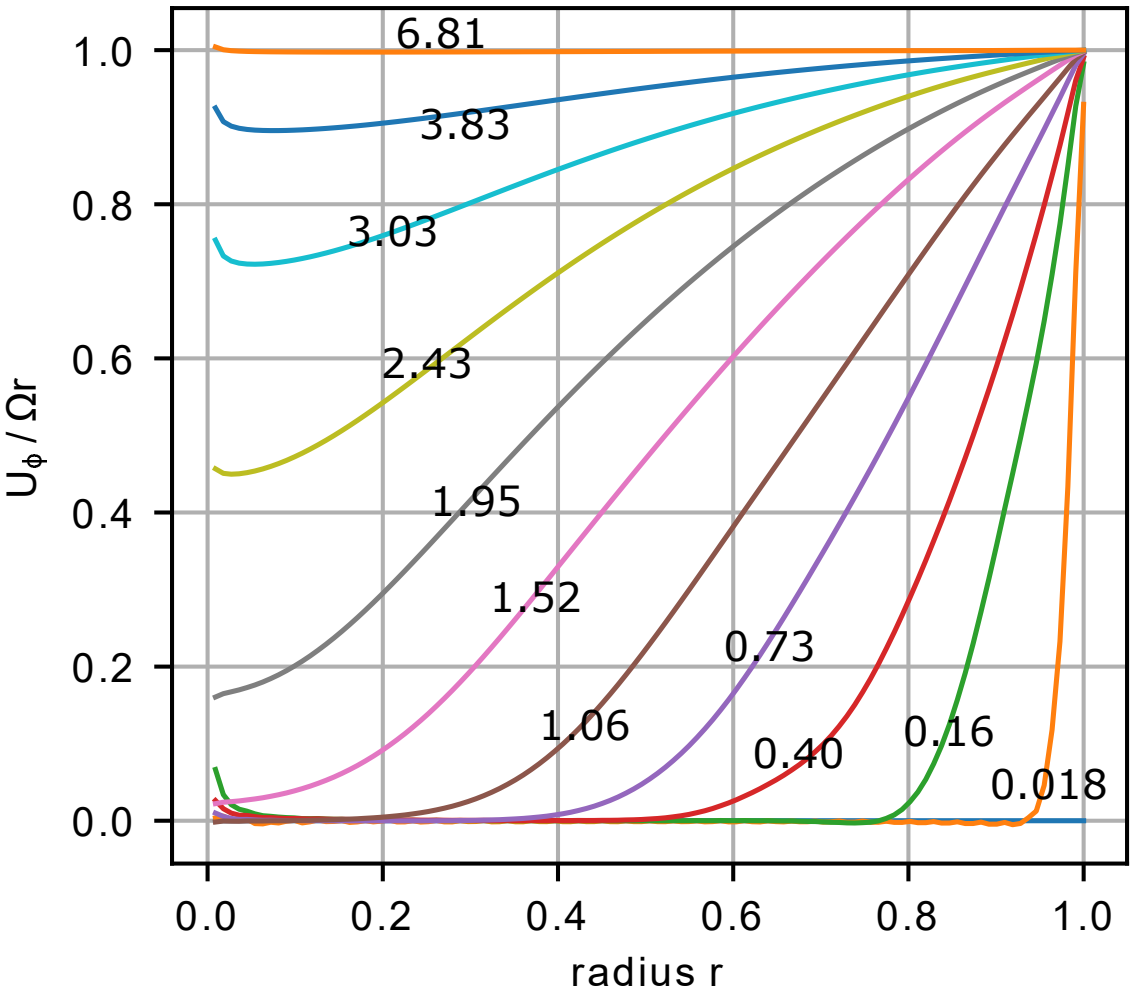

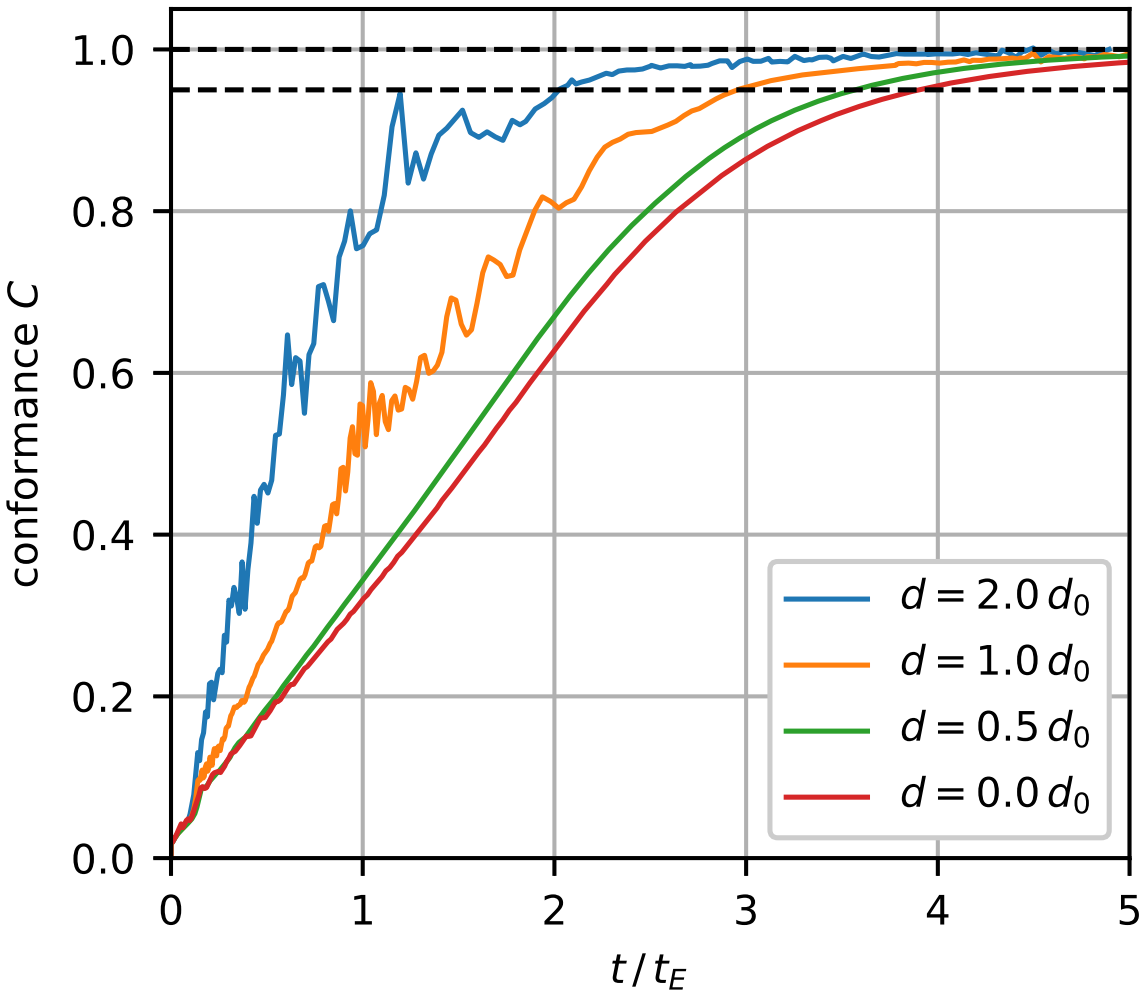

PLEASE CITE THIS ARTICLE AS DOI: 10.1063/5.0110153

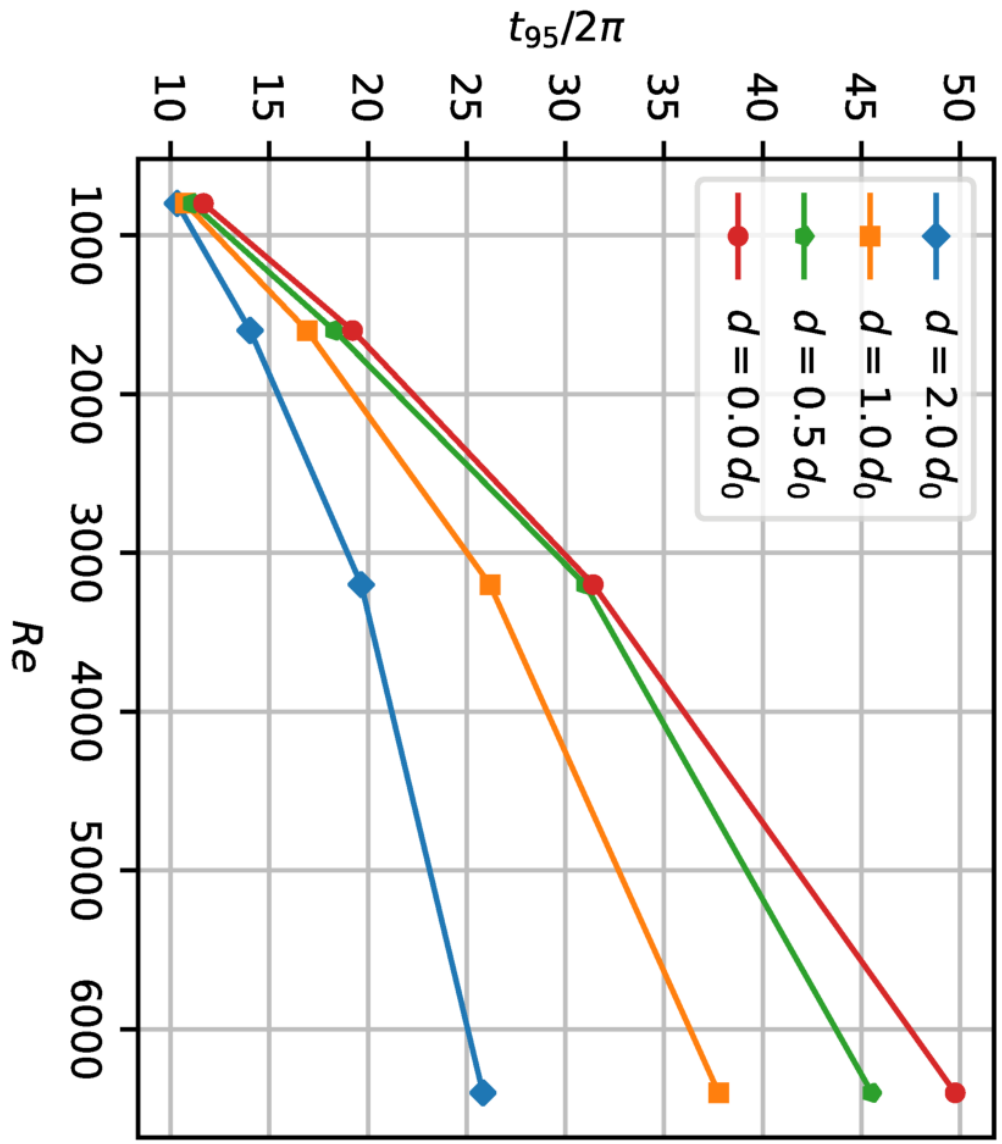

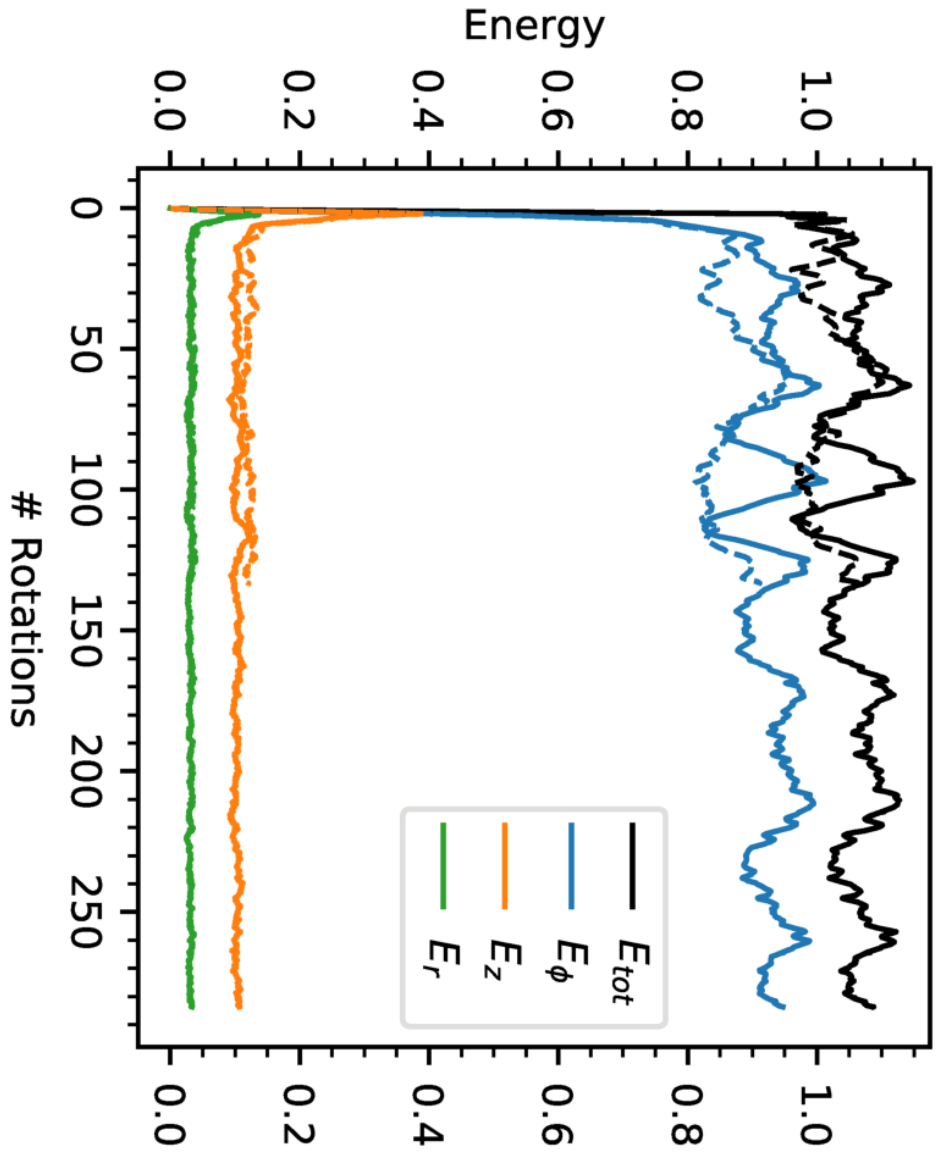

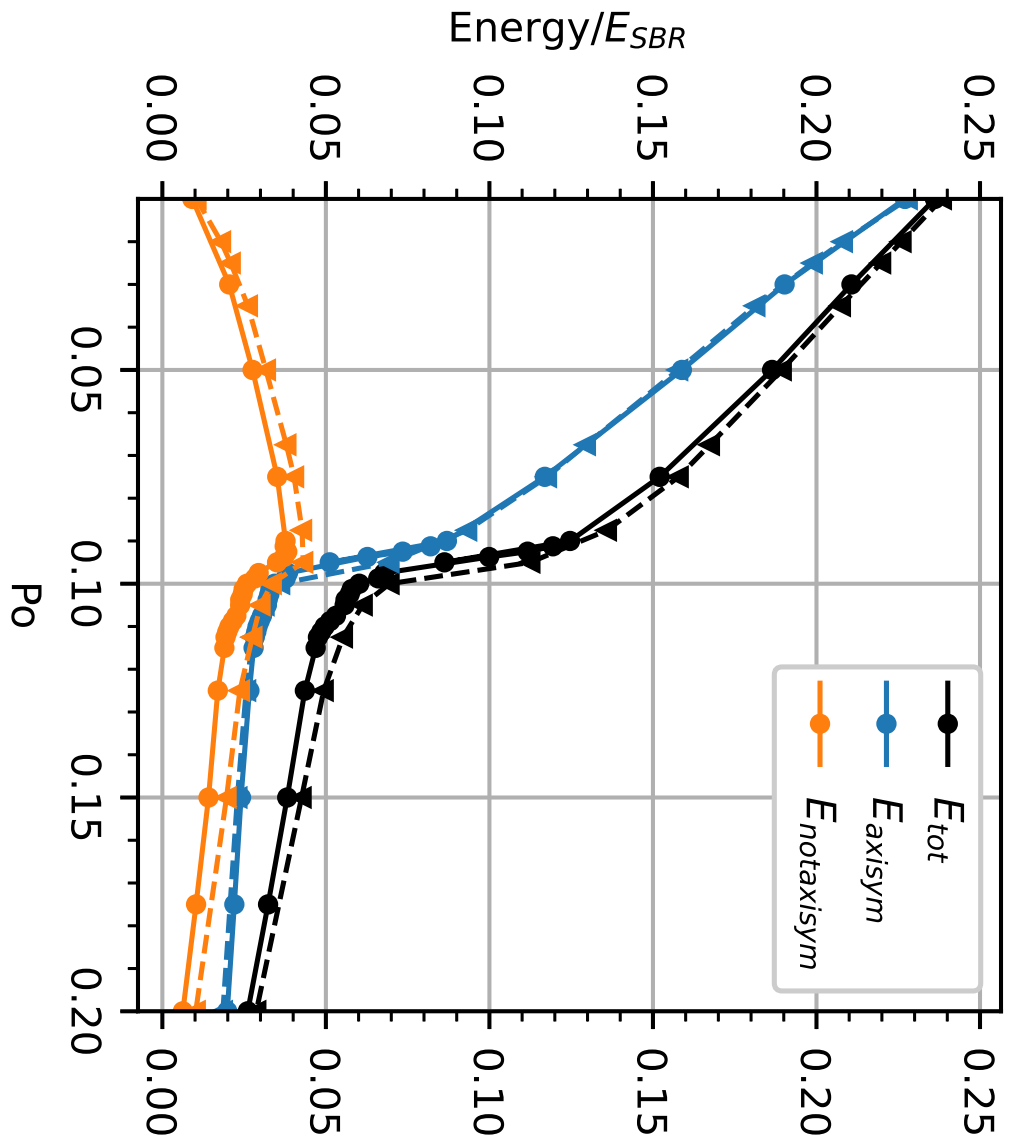

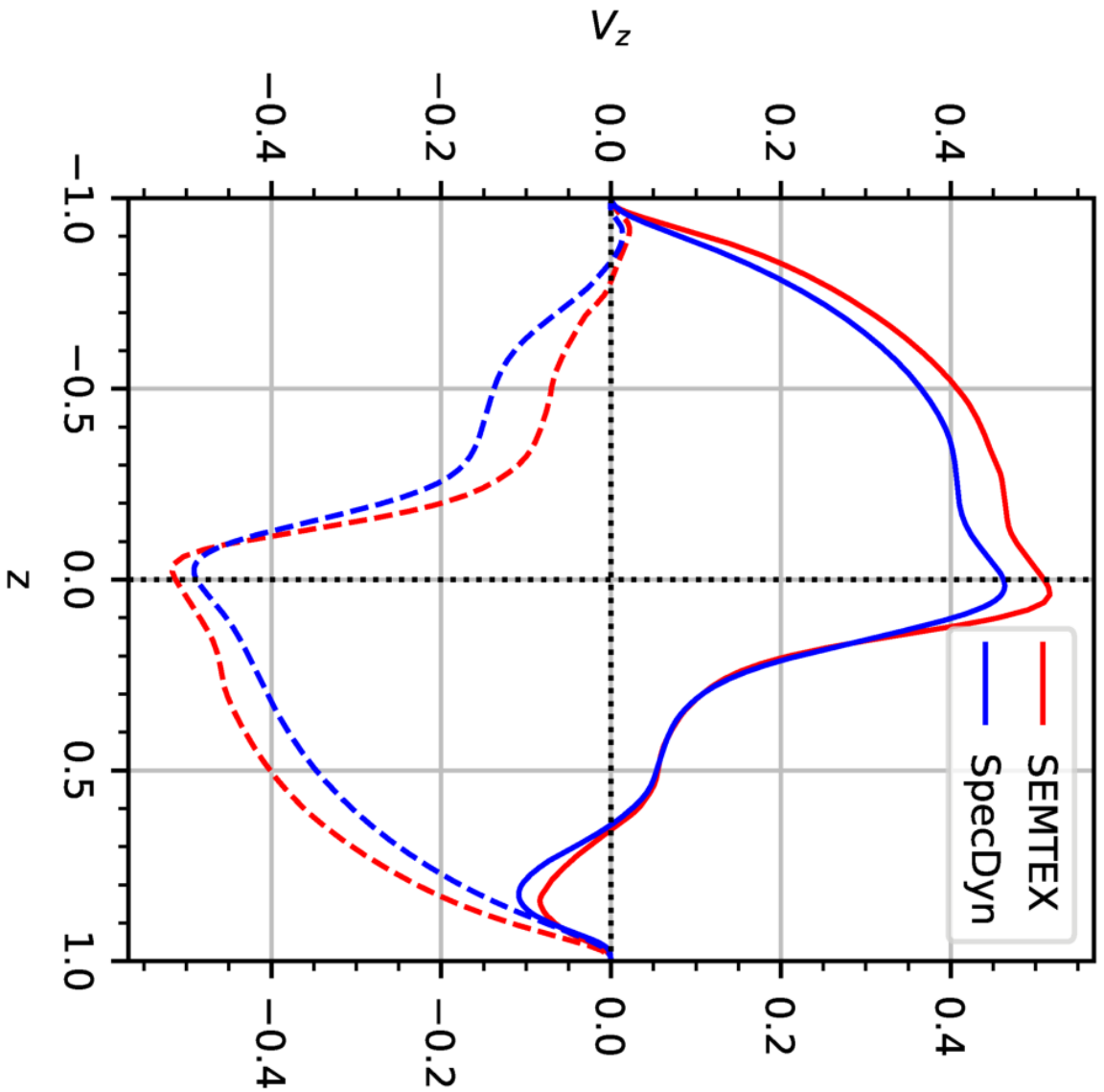

PLEASE CITE THIS ARTICLE AS DOI: 10.1063/5.0110153

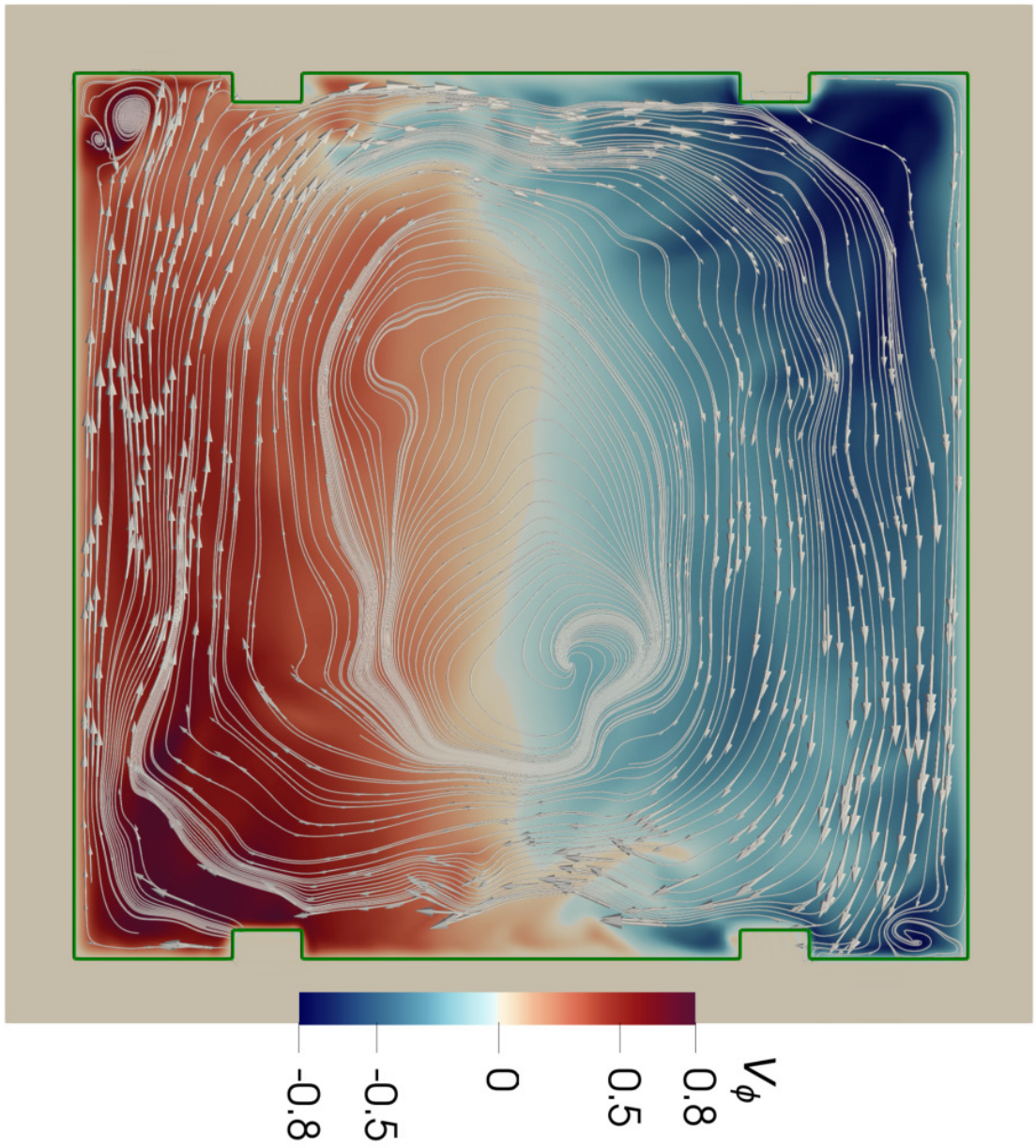

PLEASE CITE THIS ARTICLE AS DOI: 10.1063/5.0110153